Investigation of Ti-Mo mixed oxide-carbon composite supported Pt electrocatalysts: Effect of the type of carbonaceous materials

Irina Borbáth [a],[*], Emília Tálas [a], Zoltán Pászti [a], Kristóf Zelenka [a], Ilgar Ayyubov [a], Khirdakhanim Salmanzade [a], István E. Sajó [b], György Sáfrán [c], András Tompos [a]

[a] *Research Centre for Natural Sciences, Institute of Materials and Environmental Chemistry, Eötvös Loránd Research Network (ELKH), Magyar tudósok körútja 2, H-1117, Budapest, Hungary*
[b] *University of Pécs, Szentágothai Research Centre, Ifjúság u. 20. H-7624, Pécs, Hungary*
[c] *Centre for Energy Research, Institute for Technical Physics and Materials Science, Eötvös Loránd Research Network (ELKH), Konkoly-Thege M. út 29-33, H-1121, Budapest, Hungary*

ARTICLE INFO

ABSTRACT

$Ti_{0.8}M_{0.2}O_2$-C composites are novel supports for Pt-based fuel cell electrocatalysts with enhanced stability and CO-tolerance. In this work the effect of the type of the carbonaceous material (Vulcan XC-72, Black Pearls 2000 and graphite oxide) as well as the mixed oxide/carbon ratio was explored on the structure and the electro-chemical performance of the supports and the related electrocatalysts. The composites were prepared by opti-mized routes tailored to the special features of the carbonaceous materials.

Better CO tolerance was obtained on the catalysts containing 75 wt.% of the $Ti_{0.8}Mo_{0.2}O_2$ as compared to those with high carbon content. However, the more homogeneous microstructure of the catalysts with high carbon content (75 wt.%) was identified as the key for enhanced long-term stability. Considering also the fact that the high oxide content of the catalyst increases the cell resistance, the Black Pearls-based Pt electrocatalysts with $Ti_{0.8}Mo_{0.2}O_2/C = 25/75$ ratio seem to be the most promising.

1. Introduction

Fuel cells convert chemical energy of hydrogen-rich fuels into electricity without emission of greenhouse gases. An estimated 30 % of the price of a Polymer Electrolyte Membrane (PEM) fuel cell belongs to the electrocatalysts, which requires high amounts of platinum as the active element [1].

The key requirements for prospective electrocatalysts in PEM fuel cells involve [2]: (i) high stability in the anticipated pH/potential window, (ii) high resistance against electrochemical corrosion, (iii) good electronic and proton conductivity, (iv) high specific surface area, (v) appropriate porosity for mass transfer of liquid fuels or oxygen gas and the minimization of water flooding in electrodes, and (vi) strong interaction between the Pt nanoparticles and the support.

At present, Pt/C catalysts represent the most widespread choice for PEM fuel cells even if they are prone to eletrocorrosion under the working conditions of the cell, especially during start/stop cycles. The main reason for the catalyst degradation is that the cathode potential can locally rise to values up to 1.5 V during the initial phase when the

fuel gas purging is insufficient, causing aging of the carbon support as well as the platinum nanoparticles [3,4]. Corrosion results in either Pt dissolution or oxidation of the carbon support leading to detachment, Ostwald ripening and agglomeration of platinum nanoparticles [5–7]. Another issue of the traditional Pt/C catalysts is their sensitivity towards CO poisoning [8,9]. It is therefore important to explore alternative materials that can provide improved stability and increased CO tolerance.

A novel class of TiO_2 supported Pt electrocatalysts with improved stability was developed to overcome the inherent limitations of the traditional Pt/C catalysts [10,11]. It has been demonstrated that elec-trocatalytic activity, CO tolerance and stability of platinum catalyst can be also substantially improved by doping titania with oxophilic metals such as W, Mo, Sn and Ta [12–15], but electronic conductivities of these materials are still substantially lower than those of carbon catalyst supports.

On the other hand, active carbon can be regarded as a locally graphitic material with long range disorder. The graphitic nature en-sures quite high conductivity (e.g., Vulcan XC-72: 4.5 S/cm, Black Pearls

---

2000: 2.2 S/cm [16]). Materials composed of Pt nanoparticles (NPs), TiO_2 and carbon materials are identified as efficient electrocatalysts since they combine the high conductivity of carbon and corrosion resistance of the oxide with the synergistic effect between metal oxides and Pt [17–21]. Composite support materials, such as TiO_2-C also show improved stability in accelerated aging tests [22,23].

Furthermore, it is established that functionalization of the carbonaceous support has a beneficial effect on the deposition of the metal oxide. The common procedure of functionalization consists of treatment with H_2O_2, citric acid, HNO_3, or a mixture of HNO_3 and H_2SO_4 acids [24–26]. Functionalizing the carbonaceous support with glucose, HNO_3 or mixture of HNO_3-H_2SO_4 acids facilitates the growth of uniform layer of very small TiO_2 NPs on the carbon surface [27,28]. Results obtained on Pt/TiO_2/C catalysts, prepared using glucose doped Vulcan XC-72, show superior oxygen reduction reaction (ORR) activity and better durability during accelerated stress tests [29].

Recently, new types of carbonaceous materials like carbon nanotubes (CNT), graphene, reduced graphene oxides (rGO) has been reported to provide exciting properties to TiO_2-carbonaceous composites due to their special electronic structure. Exfoliated graphite oxide (GO) with abundant oxygen-containing functional groups is a relatively cheap, promising new carbonaceous starting material for composites. These functional groups [30] provide reactive and anchoring sites for nucleation and growth of nanomaterials when TiO_2 is *in situ* prepared in the presence of GO [31]. The key point for usage of GO is its exfoliation also known as delamination. Slightly basic conditions can help to achieve large degrees of dispersion, because GO layers decorated with functional groups with the same negative charge repel each other [32]. The rapid thermal exfoliation of GO leads to rGO, which contains a strongly defective single-layer and low-layer graphene sheet and can have a specific surface area of up to 800 m^2/g [33].

Huge amount of work deals with the preparation and characterization of GO derived TiO_2–carbonaceous material composites on the field of photo- [34–37] and electrocatalysis [38–40]. A Pt/graphene-TiO_2 catalyst prepared by a microwave-assisted solvothermal method exhibited a significant improvement in activity and stability towards the ORR compared with Pt/C [41]. Enhanced methanol electrooxidation performance in single fuel cell tests was demonstrated on Pt/graphene-TiO_2 hybrid catalysts synthesized by one-pot solvothermal method [42]. A unique electrocatalyst composed of a dimensionally stable anode of graphene oxide and rGO combined with RuO_2 and TiO_2 nanoparticles has also been synthesized [43]. In the above work rGO was obtained by hydrazine reduction of GO prepared by the modified Hummers's method from graphite [43]. In fact, a significant part of the works on TiO_2-graphene composites has reported the use of rGO from GO [30].

Our concept of non-noble metal-doped TiO_2 – active carbon composite supports is based on the idea of bringing together the excellent stability and nanoparticle-stabilizing ability of TiO_2 with the good co-catalytic properties of doping metal (M = W, Mo) and with the good conductivity and large surface area of active carbon in a unique material system. We demonstrated [44,45] that exclusive incorporation of the doping metals into substitutional sites of the TiO_2 lattice is a necessary requirement for practical realization of a mixed oxide – active carbon composite as a support for electrocatalysts in PEM fuel cells. Under such circumstances the TiO_2 lattice protects the doping metal atoms from dissolution, while they can still provide CO tolerance.

In the synthesis of novel TiO_2-rutile-based $Ti_{(1-x)}M_xO_2$-C multifunctional composite support materials with predominant Pt-mixed oxide interactions [46] the focus was on diversity of compositional and synthetic variables. Slightly different multistep sol-gel-based synthesis procedures were optimized for the Mo- and the W-doped composites. Our previous studies also revealed that (i) complete incorporation of the oxophilic metal can be achieved only into the TiO_2-rutile lattice and (ii) the formation of the rutile phase TiO_2 nucleus before the high-temperature treatment is prerequisite [47,48]. We demonstrated that the catalytic properties of the system are mainly determined by the

interaction between Pt and doping transition M metals (M = W, Mo); the electrochemical studies of the Mo-doped TiO_2 - active carbon composite supported Pt catalysts were completed by model studies during which Mo was electrochemically deposited onto Pt electrodes [49].

The electrochemical stability tests revealed that the degradation rate of the composite supported electrocatalysts was much smaller than that of the Pt/C and PtRu/C catalysts [44,47,50]. Better performance of the Pt/$Ti_{0.7}M_{0.3}O_2$-C (M = W, Mo) catalysts in a single cell test device using hydrogen containing 100 ppm CO compared to the reference Pt/C and PtRu/C catalysts was also demonstrated [51].

In case of Mo-doped composite supports an upper limit for Mo dopant incorporation exists around 20–30 % [48]; dopant material used in excess of this amount segregates in form of a separate MoO_2 phase. A correlation was found between the extent of Mo incorporation and the stability of the electrocatalysts: composites with lower amount of segregated Mo-oxides showed better stability. Thus, $Ti_{0.8}Mo_{0.2}O_2$–C composites with Ti/Mo = 80/20 atomic ratio was used as an optimal composition. In our recent study [52] good CO tolerance of the catalyst was demonstrated by investigation of the impact of catalyst loading, pressure and composition of reformate gas on the PEM fuel cell performance of $Ti_{0.8}Mo_{0.2}O_2$–C composite supportedanode catalyst with 20 wt.% Pt content. We found [52] that dilution of hydrogen with CO_2 and CH_4 in reformate gas had negligible negative impact on the fuel cell performance. Switching gas composition between hydrogen and reformate shows recovery of potential after CO poisoning.

However, it is known that high oxide content in the anode catalyst layer can result in some increase of the internal resistance of the cell and as a consequence in a performance loss [53]. Thus, upon the preparation of the oxide-containing composite supports the main goal is to determine an optimal ratio between the oxide and the active carbon in the composites. In line with the requirement for lower cell resistance, literature data seems to favor composites with smaller oxide content. Unfortunately, it appears that the synthesis method used for the preparation of TiO_2 coating over carbon support has the most important influence on the electrochemical properties of the catalysts; depending on the selected synthesis method the optimal content of TiO_2 in Pt/TiO_2-C catalysts varies from 10 [54] to 40 wt.% [55] of oxide in various studies. In the Pt-Pd/C-TaNbTiO_2 catalyst, the C/TaNbTiO_2 ratio in the carbon-hybrid support 75/25 was chosen as the optimal composition, which, along with excellent electrochemical properties, had good conductivity and high specific surface area [56].

Our aim in this study is to explore the behavior of electrocatalysts prepared on $Ti_{0.8}M_{0.2}O_2$-C composite supports with different types of carbonaceous backbones and with varying mixed oxide/carbon ratio. In order to minimize the effect of the preparation route, our established method was optimized for synthesis of composites with different mixed oxide/carbon ratio using GO, Vulcan XC-72, unmodified and functionalized Black Pearls 2000 as carbon materials, while preserving the rutile structure of Mo-doped TiO_2. Then using a combination of structural, spectroscopic and electrochemical methods we analyzed the effect of the mixed oxide/carbon ratio and the different carbon materials in the support on the stability and functionality of the Pt electrocatalysts, in order to determine the optimal composition for the composite supported catalyst with 20 wt.% Pt loading.

2. Experimental

2.1. Materials

$NaOH$ and HNO_3 (65 %, a.r.) were purchased from Reanal and Molar Chemicals, respectively. Titanium-isopropoxide (Ti(O-*i*-Pr)$_4$, Aldrich, 97 %) and ammonium heptamolybdate tetrahydrate ((NH_4)$_6Mo_7O_{24} \times 4H_2O$, Merck, 99 %) were used as Ti and Mo precursor compounds. Black Pearls 2000 (**BP**) and Vulcan XC-72 (**V**), supplied by Cabot, were used as carbon materials. GO was obtained from graphite by the modified Hummers' method. In order to delaminate GO the pH of the GO

suspension was adjusted to 9 with NaOH followed by a short time (~30 min) sonication.

2.2. Preparation of composite supported catalysts

Throughout this paper the samples will be identified by a unique identifier, which contains the nominal composition of the composite materials denoted by the nominal weight percentage of the carbon with respect to the mixed oxide content, along with the type of carbon used (C = BP, V, GO or functionalized F-BP): e.g., 25V means the composite of 75 wt.% of $Ti_{0.8}Mo_{0.2}O_2$ and 25 wt.% of Vulcan carbon; in all cases the desired Ti/Mo atomic ratio was 80/20.

In our previous study [57] an optimized route for preparation of $Ti_{0.8}Mo_{0.2}O_2$-C composite supports for Pt electrocatalysts with 75/25 and 25/75 oxide/carbon mass ratio containing mixed oxide with Ti/Mo atomic ratio of 80/20 ($Ti_{0.8}Mo_{0.2}O_2$) was elaborated using commercial BP and functionalized F-BP carbon materials. In this work the same method was used for functionalization: commercial BP carbon previously pre-treated in nitrogen at 1000 °C was modified using a two-step treatment with HNO_3 and glucose (F-BP); in the composites denoted as 25F*-BP the functionalization of carbon was made without pre-treatment at 1000 °C (details of such treatments are given in the Ref. [57] and related Supplementary Material).

The preparation of the mixed oxide – carbon composites consisted of three main steps (see Fig. 1 route *A* and *B*): low temperature deposition of TiO_2-rutile nuclei on the carbon backbone completed by an aging step, introduction of the Mo precursor and incorporation of the Mo into the TiO_2-rutile crystallites using a high-temperature treatment step (HTT: Ar, 600 °C, 8 h). The main difference between the preparations of

composite materials with low (25C) and high carbon content (50C and 75C) were (i) the duration and temperature of the aging step (see Fig. 1 route *A*) as well as (ii) second addition of the cc. HNO_3 before starting the aging procedure to compensate the whole acidity of the synthesis mixture. Upon the preparation of the composites with increased carbon content ($Ti_{0.8}Mo_{0.2}O_2$/C = 50/50 and 25/75) at the end of the 4-day aging procedure and before addition of Mo precursor compound the synthesis mixture was heated up to 65 °C for 8 h. Unmodified and functionalized BP- and V-containing composite materials with different $Ti_{0.8}Mo_{0.2}O_2$/C ratios were prepared similarly (for more details see Table 1).

In order to prepare GO derived composite support with a 75:25 mixed oxide/GO mass ratio (see Fig. 1, route *B*), a transparent acidic TiO_2 colloidal solution was prepared. For exfoliation of GO NaOH solution (pH~ 14) was added to the GO suspension till its pH became ~9. This suspension was sonicated for 25 min. Then the colloidal TiO_2 solution was poured to the GO suspension quickly under vigorous stirring. After that aqueous HNO_3 solution (prepared from 0.4 mL cc. HNO_3 and 7.9 mL H_2O) was added into the slurry. The pH of the slurry was adjusted to that of TiO_2 sol with cc. HNO_3 and the reaction mixture was stirred continuously for 6 days at room temperature for aging in order to facilitate rutile nuclei formation. After six days of aging, the mixture was centrifuged. The solid part was washed three times with diluted nitric acid in order to remove the well soluble $NaNO_3$. Finally, after washing the solid was re-suspended in diluted HNO_3 of the same volume. After the removal of $NaNO_3$ the molybdenum precursor compound [$(NH_4)_6Mo_7O_{24} \times 4H_2O$] was added into the acidic slurry and it was stirred for 2 h at room temperature. After that the slurry was evaporated at 65 °C, then the evaporated sample was dried overnight in the oven at
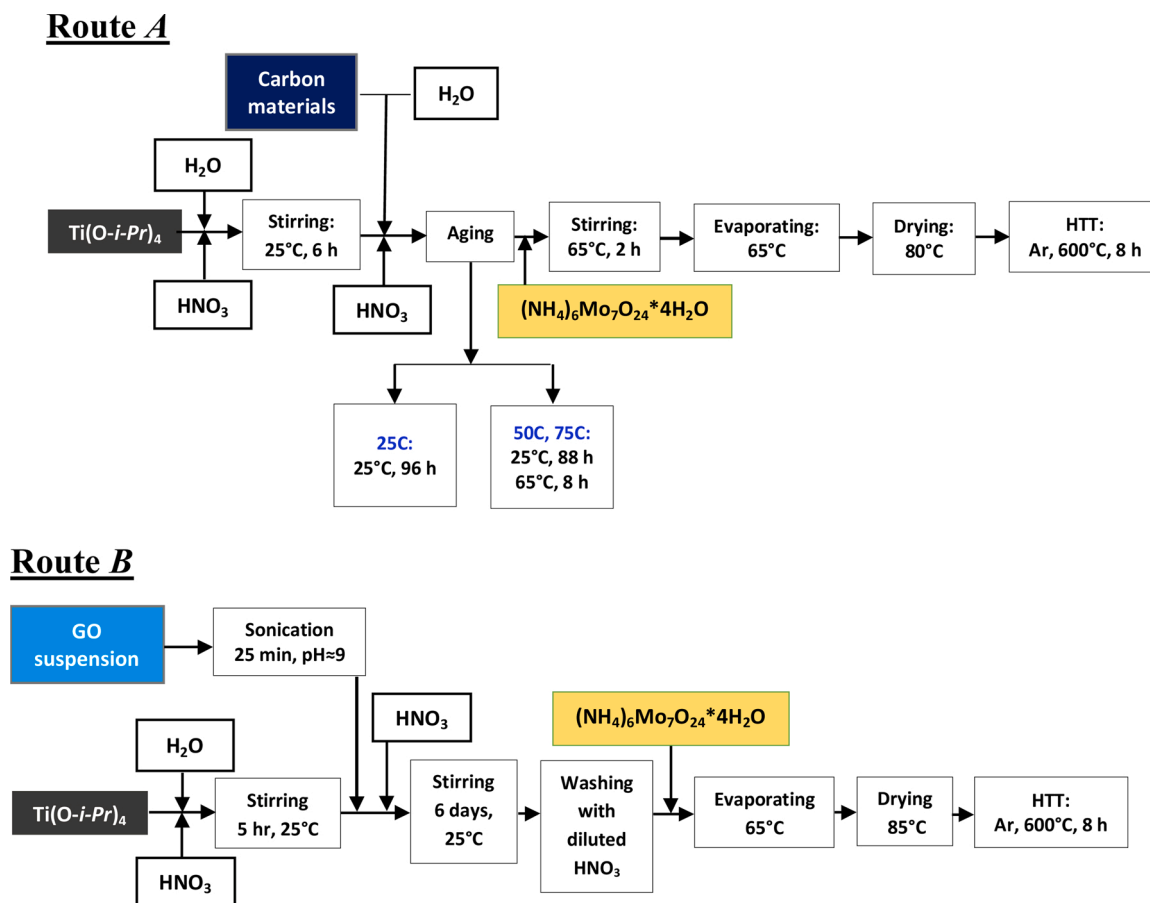

Fig. 1. Route *A:* flow chart for preparing Vulcan, unmodified and functionalized BP-containing $Ti_{0.8}Mo_{0.2}O_2$-C composite support materials with different mixed oxide/carbon mass ratio ($Ti_{0.8}Mo_{0.2}O_2$/C = 75/25 (denoted as 25C), 50/50 (50C) and 25/75 (75C)). Route *B:* flow charts for preparing GO-derived 75 wt.% $Ti_{0.8}Mo_{0.2}O_2$ – 25 wt.% C composite support materials (denoted as 25GO). HTT: high-temperature treatment.

Table 1

Nominal composition and preparation details of the carbon-containing (C = BP, F-BP and Vulcan) and GO derived composites with the different $Ti_{0.8}Mo_{0.2}O_2/C$ ratios.

№	Samples nominal composition [a]	TiO$_2$ sol			Suspension of carbon			Mo prec.[b](g)
		H$_2$O (ml)	HNO$_3$ (ml)	Ti prec.[b] (ml)	C (g)	H$_2$O (ml)	HNO$_3$[c] (ml)	
25C	75Ti$_{0.8}$Mo$_{0.2}$O$_2$-25C	21	2.35	2.05	0.25	10	–	0.2989
50C	50Ti$_{0.8}$Mo$_{0.2}$O$_2$-50C	14	1.55	1.36	0.50	12.5	0.39	0.1993
75C	25Ti$_{0.8}$Mo$_{0.2}$O$_2$-75C	7	0.78	0.68	0.75	15	0.78	0.0997
25GO	75Ti$_{0.8}$Mo$_{0.2}$O$_2$-25C	21	1.11	0.79	0.17[d]	–	–	0.1172

[a] Expected composition of composites with different $Ti_{0.8}Mo_{0.2}O_2/C$ mass ratio.
[b] Ti and Mo precursor compounds: $(Ti(O\text{-}i\text{-}Pr)_4$ and $(NH_4)_6Mo_7O_{24} \times 4H_2O)$.
[c] cc. HNO$_3$ (65 %, Molar Chemicals, a.r.).
[d] GO in a suspension of 0.95 wt.%, pH adjusted to 9 with NaOH solution.

85 °C. As a final step of the synthesis of the catalyst support material, HTT at 600 °C in Ar atmosphere was performed for the molybdenum incorporation.

The BP-, V- and GO-containing support materials were loaded with 20 wt.% Pt via a modified, sodium borohydride (NaBH$_4$) assisted ethylene-glycol (EG) reduction-precipitation method in order to obtain platinum containing electrocatalyst (for further details see our earlier works [48,57]).

2.3. Physicochemical characterization

X-ray powder diffraction (XRD) patterns were obtained in a Philips model PW 3710 based PW 1050 Bragg-Brentano parafocusing goniometer using CuKα radiation (λ = 0.15418 nm), graphite monochromator and proportional counter. Silicon powder (NIST SRM 640) was used as an internal standard. Lattice parameters were determined using a full profile fit (Pawley-fit) [58]. The cell parameters of the crystalline phases were determined from the fitted values.

Nitrogen adsorption measurements were carried out at temperature of liquid nitrogen using Thermo Scientific Surfer automatic volumetric adsorption analyzer (Thermo Fischer Scientific, Berlin, Germany). The specific surface area was calculated by the BET method in the range of relative pressures from 0.05 to 0.30.

Transmission Electron Microscopy (TEM) studies of the samples were made by use of a JEOL 3010 high resolution transmission electron microscope operating at 300 kV. Particle size of composite supported Pt catalysts were determined by measuring the diameters of no less than 900 randomly selected metal particles in at least ten micrographs of each sample taken from non-aggregated areas using the ImageJ software.

X-ray photoelectron spectroscopy (XPS) measurements were performed using an electron spectrometer manufactured by OMICRON Nanotechnology GmbH (Germany). MgKα (1253.6 eV) radiation was used as excitation source and data were acquired with 1 eV spectral resolution (30 eV pass energy). The powdered composite supports and catalysts were suspended in isopropanol or hexane and drops of this suspension were dried onto stainless steel sample plates. Spectra were processed with the CasaXPS package [59] by fitting the measured data with a combination of Gaussian-Lorentzian product peaks over a Shirley-type background, while quantitative evaluation of the data was performed with the XPSMultiQuant package [60,61] during which a homogeneous depth distribution was assumed for all components. Chemical states were identified using the NIST database [62], the publication [63] or other literature as indicated. Binding energies were referenced to the lowest binding energy contribution of the C 1s envelope, which was assigned to graphite-like (sp^2-hybridized) carbon in the carbon backbone (284.4 eV).

2.4. Electrochemical characterization

A Biologic SP 150 potentiostat and a standard three-electrode electrochemical cell were used for the electrochemical measurements. The applied electrolyte was 0.5 M H$_2$SO$_4$ solution, which was prepared by using Milli-Q water and concentrated H$_2$SO$_4$.

Glassy carbon (GC; d=0.3 cm) electrode with 0.0707 cm^2 surface area was used as working electrode. Platinum wire was used as counter electrode and a hydrogen electrode as reference electrode. All potentials are given on RHE scale. The details of the working electrode preparation, the catalyst ink composition and electrocatalytic measurements were described in Refs. [45,48]. The Pt loading of the electrodes was 10 μg cm^{-2}. Taking into account the possible inhomogeneity of the samples, usually at least three independent electrochemical measurements were carried out.

Electrocatalytic performance of the 20 wt.% Pt/Ti$_{0.8}$Mo$_{0.2}$O$_2$-C electrocatalysts was studied by cyclic voltammetry and CO$_{ads}$-stripping voltammetry measurements combined with stability test involving 500 polarization cycles and the second CO$_{ads}$-stripping voltammetry measurement. In the long-term stability test, the samples were submitted to cyclic polarization at a 100 mV s^{-1} scan rate for 10,000 cycles between 50 and 1000 mV potential limits; these measurements took ca. 54 h.

The charges associated with hydrogen underpotential deposition, Q$_{oxHupd}$, were calculated using conventional baseline correction. From the oxidation charge of the monolayer hydrogen the electrochemically active Pt surface area (ECSA$_{Hupd}$) can be calculated using the Eq. 1 [64]:

$$ECSA_{Hupd} \ (cm^2) = Q_{oxHupd} \ (\mu C) \ / \ 210 \ (\mu C/cm^2), w \tag{1}$$

here ECSA$_{Hupd}$ is the electrochemical surface area determined from the amount of underpotentially deposited hydrogen on the platinum surface; Q$_{oxHupd}$ is the oxidation charge of underpotentially deposited hydrogen obtained from the CV experiment and 210 (μC/cm^2) is the amount of charge required to oxidize monolayer hydrogen adsorbed on 1 cm^2 of polycrystalline platinum surface.

Results concerning on the change of the electrochemically active Pt surface area upon the N-cycle stability test are presented as ECSA$_N$ (N: 500, 2,500, 5000 and 10,000) normalized to ECSA$_1$ measured in the first cycle on the same sample. Another measure of the change of the electrochemically active Pt surface area is the ΔECSA value defined in Eq. 2 [57]:

$$\Delta ECSA_N = \{1-(ECSA_N/ECSA_1)\} \times 100 \ \% \tag{2}$$

After every stability test the electrolyte was changed to fresh one to avoid the re-deposition of the dissolved metals. Electrochemical performance of the Pt/Ti$_{0.8}$Mo$_{0.2}$O$_2$-C electrocatalysts was compared with that of 20 wt.% Pt/C (Quintech) commercial one.

3. Results and discussion

3.1. Influence of the phase composition and microstructure of the composites on the electrochemical performance of the related Pt catalysts. Preliminary results

In the Introduction we emphasized the importance of the exclusive formation of the rutile mixed oxide phase on the carbon and the good incorporation of Mo in order to get stable electrocatalysts. Without adaption of the synthesis procedure to the surface chemical features of

the carbon material, often a mixture of rutile and anatase was formed, sometimes along with excessive segregation of Mo-oxides. In this section XRD and electrochemical results obtained on catalysts with multiple oxide phases will be discussed in order to justify our efforts for optimization of the composite preparation.

Fig. 2A shows the XRD patterns obtained on $Ti_{0.8}Mo_{0.2}O_2$-C composite materials prepared using HNO_3 and glucose functionalized BP carbon, with (25F-BP) and without previous treatment in nitrogen at 1000 °C (25F*-BP). As can be seen in Fig. 2A in the case of the 25F-BP sample only the reflections of the TiO_2-rutile crystallites were observed, but in the 25F*-BP sample the mixture of the TiO_2-rutile and anatase phases was detected.

According to our previous studies [57], the percentage of the surface oxygen functional groups (FGs) of the HNO_3-glucose functionalized BP carbon materials and the BET surface area of the corresponding composites were quite similar, irrespectively to the pre-treatment of carbon at 1000 °C (FG = 19.5 and 22 % and S_{BET} = 135 and 147 m^2/g for the 25F*-BP and 25F-BP, respectively). However, the ratio between the surface oxygen FGs decomposed below and above 500 °C was different; pre-treatment of carbon at 1000 °C resulted in higher content of the FGs decomposed above 500 °C [57]. It has been demonstrated in our previous studies [48,51] that preliminary formation of the rutile-TiO_2 phase in the presence of carbon at room temperature (RT) is prerequisite for complete dopant (Mo, W) incorporation into the TiO_2 lattice upon high-temperature treatment. In order to facilitate the formation of rutile nuclei, the duration of the RT aging of the Ti-sol in the presence of carbon and the acidity of the synthesis mixture were optimized. However, when using composite materials prepared with various functionalized carbons, one more variable should be considered: despite using the same preparation procedure, it is likely that various surface oxygen FGs of different character (hydroxyl, carboxylic, lactone, ether groups, etc. [57]) have different influence on the deposition of TiO_2 nuclei on the carbon backbone during the first preparation step, resulting in exclusive formation of TiO_2-rutile or mixture the rutile and anatase phases.

According to the literature [65–67] and our recent study [57], the mass losses in the low temperature range from 200 to 500 °C on the TGA curves of the samples treated with (HNO_3 + glucose) can be related (i) to elimination of hydroxyl and carboxyl groups (227 °C and 273 °C, respectively) as well as (ii) to the decomposition of the stronger chemical bonds in glucose (337 °C). Thus, it can be concluded that the presence of higher content of the FGs decomposed below 500 °C has negative influence on the exclusive formation of TiO_2-rutile.

Moreover, we demonstrated [57] that the major part of the FGs (65 %) of carbon functionalized without pre-treatment at 1000 °C can be eliminated upon treatment in N_2 at 500 °C for 1 h. Since for incorporation of Mo into rutile lattice treatment at 600 °C is needed [48,51], the presence of higher content of FGs, which decomposed above 500 °C, can be beneficial for the increase of the composite stability. In this respect, the final dispersion of deposited metal oxides and resistance to sintering are more negatively affected by the presence of the less stable FGs.

As derived from the CV-s in Fig. 2.C, during the 500-cycle stability tests very small performance loss was observed on both catalysts (7,0 % and 12.6 % on the Pt/25F-BP and Pt/25F*-BP, respectively, see also Fig. 2B). Electrochemically active Pt surface area calculated from the CVs of fresh catalysts was 60.9 m^2/g_{Pt} and 58.9 m^2/g_{Pt} for the Pt/25F-BP and Pt/25F*-BP, respectively. Moreover, very similar behaviour in the CO_{ads} stripping measurements (Fig. 2D) was observed on both electrocatalysts. However, according to the results of the 10,000-cycle longterm stability test (see Fig. 2B) pronounced difference was observed between the two catalysts: the ΔECSA values calculated for the Pt/25F-BP and Pt/25F*-BP catalysts were 30.5 and 54.2 %, respectively. These results clearly demonstrate that the presence of the mixed oxide in the form of different crystalline phases in the composite materials negatively affects the long-term stability of the corresponding catalyst.

In the next set of experiments $Ti_{0.8}Mo_{0.2}O_2$-C composite supported catalysts with high mixed oxide content prepared using unmodified (25V) and HNO_3-glucose-functionalized Vulcan (25F-V) were compared
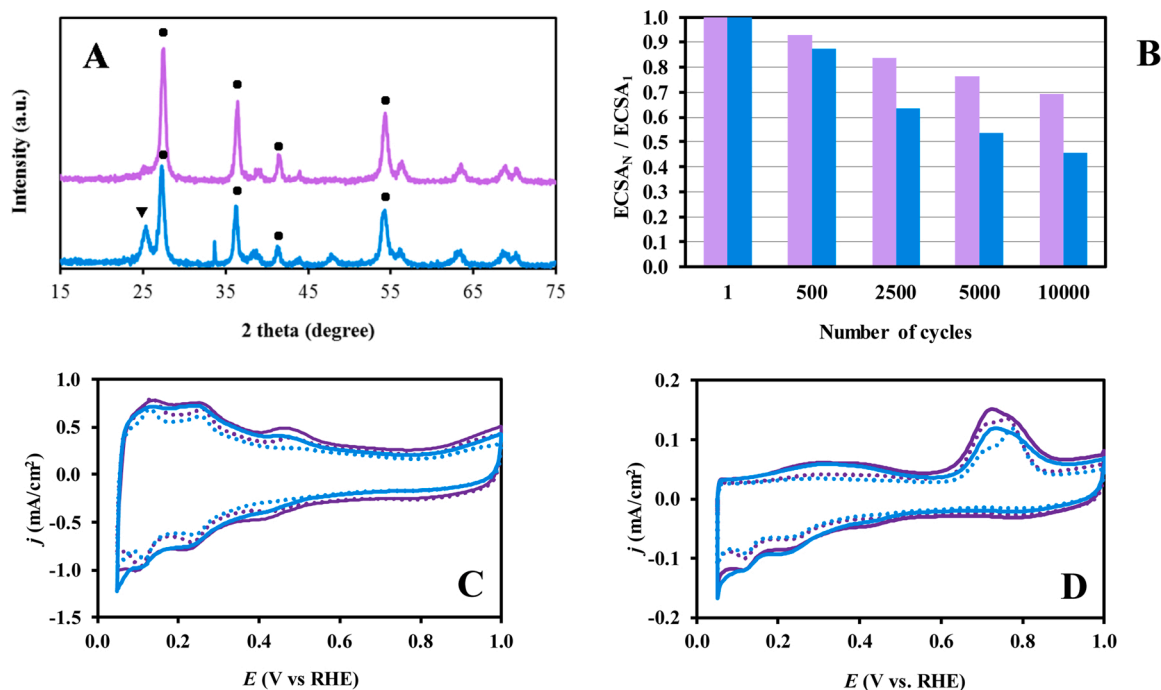

Fig. 2. (A) XRD patterns of functionalized BP-containing $Ti_{0.8}Mo_{0.2}O_2$-C composites (25F-BP (■) and 25F*-BP (■)) after HTT; ●- rutile, ▼- anatase. (B) Comparison of the electrochemically active Pt surface measured after N cycles normalized to ECSA measured in the 1st cycle ($ECSA_N$/$ECSA_1$) of the Pt/25F-BP (■) and Pt/25F*-BP (■) catalysts as a function of the number of cycles (N). (C) CVs and (D) CO_{ads} stripping voltammograms of the Pt/25F-BP and Pt/25F*-BP catalysts recorded before (solid line) and after 500 cycles (dotted line) of the stability test. Obtained in 0.5 M H_2SO_4 at 100 mV/s (C) and 10 mV/s (D), T=25 °C. Preparation details of the functionalization of BP carbon are given in Ref. [55].
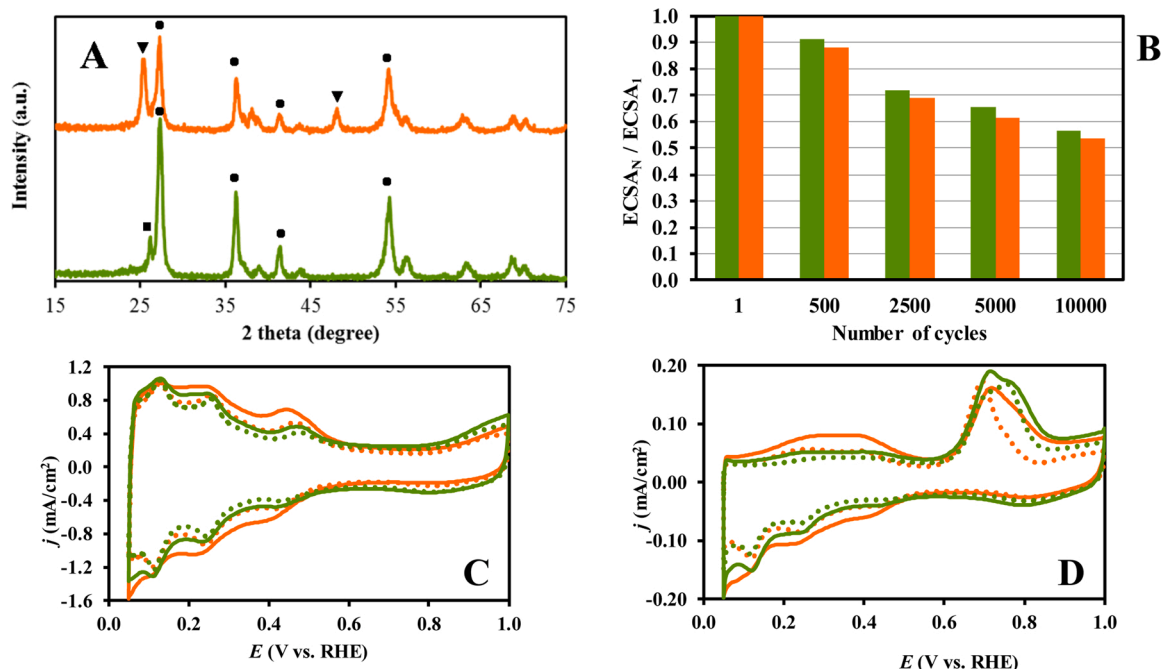
Fig. 3. (A) XRD patterns of Vulcan-containing $Ti_{0.8}Mo_{0.2}O_2$-C composites (25V (■) and 25F-V (■)) after HTT; ●- rutile, ▼- anatase, ■- MoO_2. (B) Comparison of the electrochemically active Pt surface area measured after N cycles normalized to ECSA measured in the 1st cycle ($ECSA_N/ECSA_1$) of the Pt/25V (■) and Pt/25F-V (■) catalysts as a function of the number of cycles (N). (C) CVs and (D) CO_{ads} stripping voltammograms of the Pt/25V and Pt/25F-V catalysts recorded before (solid line) and after 500 cycles (dotted line) of the stability test. Obtained in 0.5 M H_2SO_4 at 100 mV/s (C) and 10 mV/s (D), T=25 °C.

(Fig. 3).

In our recent study it has been demonstrated [57] that functionalization of carbon, resulting in a more uniform mixed oxide coating, unfortunately leads to a marked decrease in the specific surface area (SSA) and total pore volume of the composite support materials; in addition, the higher the oxide content, the more pronounced the decrease in surface area. Thus, the lowest value of the $S_{BET} = 147 \ m^2/g$ was obtained for the functionalized F-BP-based composite with 75 wt.% of mixed oxide (see 25F-BP in Table 2). Unfortunately, the use of Vulcan as a carbon source in the preparation of composites with high mixed oxide content (see sample 25V in Table 2) results in materials with surface area below the recommended value for electrocatalyst support (100 m^2/g). Moreover, our results showed that a decrease of the surface area of the composite largely hinders the incorporation of Mo into the TiO_2 lattice. According to XRD pattern of the 25V composite studied after HTT the reflections of the TiO_2-rutile were found together with minor

amount of the MoO_2 crystalline phase (see Fig. 3A). However, a mixture of the TiO_2-rutile with relatively big amount of anatase phases was detected in the 25F-V sample (see Fig. 3A). It is necessary to mention that according to our previous results the TiO_2-anatase phase is not suitable for Mo doping with our technique [48,57]. Consequently, the presence of certain amount of unincorporated amorphous MoO_2 located on the surface of the composite support can be expected.

Despite the low surface area of the composite materials high ECSA calculated from CVs (Fig. 3C) and relatively small ΔECSA in the 500-cycle stability test were obtained for both catalysts (ECSA = 81.3 m^2/g_{Pt} and 88.4 m^2/g_{Pt}; ΔECSA = 9.0 and 12.2 % for the Pt/25V and Pt/25F-V, respectively).

The CO electrooxidation (the so-called "pre-peak") started on both catalysts at ca. 50 mV (see Fig. 3D). As shown in Fig. 3D the main difference observed on these two catalysts was the intensity of the "pre-peak" area; quite pronounced "pre-peak" area was characteristic for the

Table 2
Characterization of the $Ti_{0.8}Mo_{0.2}O_2$-C composites and the related Pt catalysts by TEM, XRD and nitrogen adsorption measurements.

Sample	Nominal composition	C type [a]	S_{BET}, m^2/g [b]	Pore volume, cm^3/g [b]	Pt size, nm (TEM)	Lattice parameters, Å [c]	Mo subst., %	Pt, % (XRD)
25BP	$75Ti_{0.8}Mo_{0.2}O_2$-25C	BP	248 [d]	0.51	2.9 ± 0.8 [d]	a= 4.630, c= 2.940	18	–
50BP	$50Ti_{0.8}Mo_{0.2}O_2$-50C	BP	411	1.02	2.3 ± 0.5	a= 4.630, c= 2.940	18	–
75BP	$25Ti_{0.8}Mo_{0.2}O_2$-75C	BP	1120 [d]	2.01	2.7 ± 0.7 [d]	a= 4.630, c= 2.940	18	–
25F-BP	$75Ti_{0.8}Mo_{0.2}O_2$-25C	F-BP	147 [d]	0.39	2.5 ± 0.6 [d]	a= 4.630, c= 2.940	18	–
50F-BP	$50Ti_{0.8}Mo_{0.2}O_2$-50C	F-BP	455	0.81	3.1 ± 0.7	a= 4.630, c= 2.940	18	–
75F-BP	$25Ti_{0.8}Mo_{0.2}O_2$-75C	F-BP	726 [d]	1.32	2.8 ± 0.7 [d]	a= 4.630, c= 2.940	18	–
25V	$75Ti_{0.8}Mo_{0.2}O_2$-25C	V	47	0.28	2.0 ± 0.6	a= 4.630, c= 2.940	18	–
50V	$50Ti_{0.8}Mo_{0.2}O_2$-50C	V	108	0.38	2.4 ± 0.6	a= 4.630, c= 2.940	18	–
75V	$25Ti_{0.8}Mo_{0.2}O_2$-75C	V	175	0.48	2.0 ± 0.6	a= 4.630, c= 2.940	18	–
25GO	$75Ti_{0.8}Mo_{0.2}O_2$-25C	GO	130	0.39	2.4 ± 0.9	a= 4.640, c= 2.935	23	–
Pt/25GO	20 Pt/$75Ti_{0.8}Mo_{0.2}O_2$-25C	GO	–	–	2.4 ± 0.9	a= 4.640, c= 2.935	23	17.1
Pt/25BP	20 Pt/$75Ti_{0.8}Mo_{0.2}O_2$-25C	BP	–	–	2.9 ± 0.8	a= 4.630, c= 2.940	18	21.4

[a] **BP**: Black Pearls 2000, **V**: Vulcan; **GO**: Graphite Oxide derived carbon; **F-BP**: BP carbon pre-treated at 1000 °C in nitrogen for 3 h before functionalization, then functionalized with HNO_3 and glucose.

[b] Specific surface area and total pore volume of the composite support materials determined by nitrogen adsorption measurements.

[c] Lattice parameters of the rutile phase obtained after HTT; Pure rutile TiO_2: a=4.593 Å, c= 2.959 Å.

[d] From Ref. [57].

Pt/25F-V catalyst. We demonstrated earlier [45] that only CO adsorbed on specific Pt sites, where Pt and Mo atoms are in atomic closeness, can be oxidised below 400 mV potential. Thus, taking into account the high intensity of the "pre-peak" area it can be assumed that the number of MoO_x particles in the close vicinity of the Pt in the Pt/25F-V catalyst may be higher. It is necessary to mention that the intensity of Mo redox peak pair observed on this sample was also higher comparing to the Pt/25V catalyst as shown in Fig. 3C.

Nevertheless, the stability of these catalysts is among the worst compared to the other ones studied in this work. Significant degradation was observed on both catalysts after 10,000 polarization cycles: $\Delta ECSA$ = 43.6 and 46.5 % for the Pt/25V and Pt/25F-V catalysts, respectively. Apart from the complicated phase composition, the fast degradation seems also to be connected to the low SSA of the Vulcan-containing composite. This issue will be further discussed at the end of the paper.

These results demonstrate that not only the phase composition, but also the surface area of the catalyst support, especially that of its mixed oxide part, plays an important role in the development of promising electrocatalysts.

3.2. Characterization of the $Ti_{0.8}Mo_{0.2}O_2$-C composites and the related Pt catalysts by XRD. Optimization of the preparation procedure

As was mentioned above the main goal of this study was to use Vulcan, BP and GO as carbon materials to develop the synthesis of a composite with different mixed oxide/carbon ratio and rutile structure of Mo-doped TiO_2 to create highly efficient and stabile electrocatalysts with an optimal ratio between $Ti_{0.8}Mo_{0.2}O_2$ and carbon.

In order to adapt the composite preparation method for GO, we had to overcome the difficulty that strong acidic media is necessary for the formation of the rutile nuclei (consequently to Mo incorporation), whereas mild basic media is necessary for the delamination of GO. During the preparation we choose the strong acidic media (0.69 M HNO_3) to form rutile nuclei and we added the delaminated solution of GO (pH adjusted to 9 with NaOH) suddenly to the reaction mixture by use of vigorous stirring. The original pH was then restored with cc. HNO_3 (see Fig. 1B in Experimental part). According to the XRD pattern of the samples obtained after the drying step at 85 °C and before HTT this procedure resulted in rutile nuclei beside the amorphous part (see Fig. 4A). Subjecting these samples to HTT, further crystallization occurred. After HTT the XRD patterns of the 25GO samples showed the presence of rutile phase with trace of the MoO_2 phase (Fig. 4A).

Literature dealing with rutile-based mixed oxides indicates that W- or Mo-incorporation results in a characteristic distortion of the rutile-TiO_2 cell [68] and the change in the cell parameters measured by X-ray diffraction can be used for characterization of the amount of incorporated doping cations. According to this, changes of lattice parameters presented in Table 2 (a = 4.640, c = 2.935 Å, while pure rutile TiO_2 structure has a = 4.593 Å, c = 2.959 Å) indicated 23 % of Mo substitution

for the mixed oxide – GO composite. It should be noted that the degree of Mo incorporation (calculated Mo_{subst} = 23 %) was higher than the nominal Mo content (nominal Mo_{subst} = 20 %) only in case of the GO derived composite materials. The application of the additional washing step with diluted nitric acid for $NaNO_3$ removal before the introduction of the Mo precursor compound was a distinctive feature of the synthesis of GO-based composite materials. As a result, certain part of TiO_2-rutile nuclei, deposited onto the carbon backbone may have been removed. Consequently, the real Ti/Mo ratio could be smaller than the nominal one. According to our previous studies upon the preparation of the composite support containing mixed oxide with Ti/Mo ratio of 80/20 and 70/30 the degree of Mo incorporated into the unit cell was 21 and 25 %, respectively [48]; based on above results, the actual Ti/Mo ratio during the GO-based synthesis could be between 80/20 and 70/30.

Broad reflections at 2 theta values of 39.6, 47.4, 67.1°, arise from the (111), (200), and (220) planes of the fcc structure of platinum, respectively [69]. The broad diffraction peaks indicate the presence of nano-dispersed Pt crystallites in the Pt/25GO catalyst (Fig. 4A).

As shown in Fig. 4B only the reflections of the TiO_2-rutile crystallites were observed in the XRD pattern of the 25V composite studied before HTT; no reflections characteristic to Mo oxides were found. However, after HTT the reflections of the TiO_2-rutile and very small amount of MoO_2 crystalline phase were detected (see Fig. 4B). The characteristic distortion in the lattice parameters of the rutile phase obtained after HTT on the 25V composite (a = 4.630 Å, c = 2.940 Å, see Table 2) confirmed the incorporation of Mo into TiO_2-rutile lattice with Mo_{subst} = 18 %. It should be noted that the relatively small surface area of Vulcan can be a reason of the presence of some amount of unincorporated MoO_2 crystalline phase (especially in the case of the V-based composites with high oxide content (25V)).

Therefore, in the preparation of Vulcan-containing composites, one more step was added: after introduction of the Mo precursor compound the synthesis mixture was treated at 65 °C under continuous stirring for additional 2 h; then, as usual, the solvent was evaporated overnight at 65 °C. Our experience shows that the addition of this new step results in pronounced decrease of the reflections characteristic to the crystalline MoO_2 phase. As shown in Fig. 1 (route **A**), the preparation of all composites presented in this study was done with the inclusion of this additional treatment.

As shown in Fig. 4B the deposition of platinum resulted again in the appearance of the broad lines characteristic to the reflections of very small Pt crystallites.

The influence of the type of carbonaceous material on the structure and composition of the 25C (C= BP, V and GO) composite supported Pt catalysts was demonstrated in Fig. 5A. As shown in Fig. 5A taking into account the peculiarities of various carbonaceous materials optimal synthesis method was developed for the preparation of the 25C composites with high mixed oxide content and total Mo incorporation into the rutile-TiO_2 lattice; no reflections characteristic to unincorporated
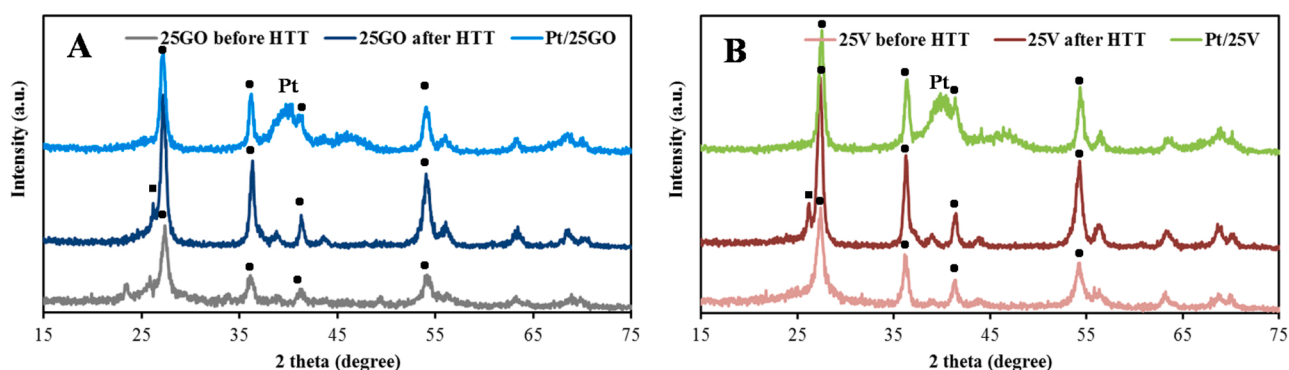

Fig. 4. XRD patterns of the GO- (A) and Vulcan-containing $Ti_{0.8}Mo_{0.2}O_2$-C composites (B) with low carbon content (25C) before and after HTT as well as after Pt loading. ●- Rutile, ■- MoO_2.
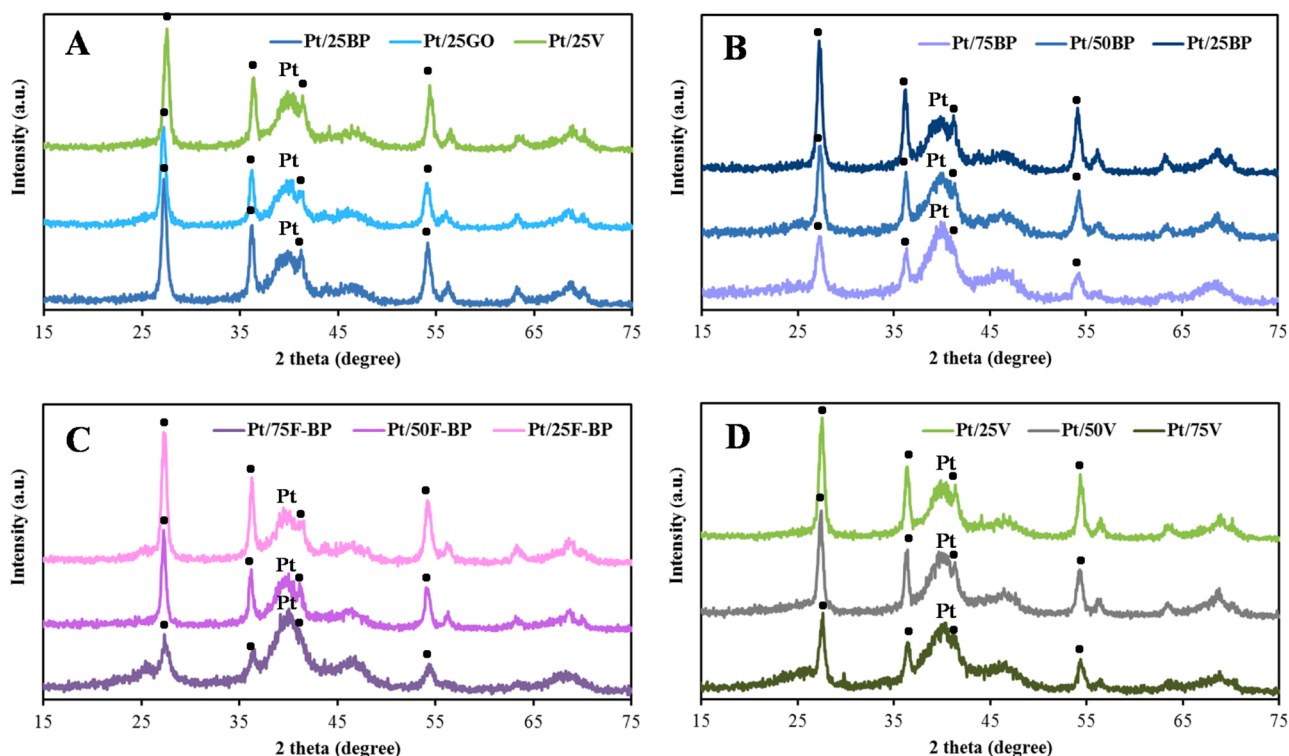
Fig. 5. XRD patterns of Pt/Ti$_{0.8}$Mo$_{0.2}$O$_2$-C catalysts: (A) Influence of the type of carbonaceous material used on the structure of the 25C (C= BP, V and GO) composite supported Pt catalysts. Influence of the Ti$_{0.8}$Mo$_{0.2}$O$_2$/C ratios (Ti$_{0.8}$Mo$_{0.2}$O$_2$/C = 75/25, 50/50 and 25/75) in the composite supports containing BP (B), F-BP (C) and Vulcan (D) on the structure of Pt catalysts. ●- Rutile.

MoO$_x$ oxides were found. Moreover, in all Pt/25C catalysts the platinum is present in nanodispersed form. As seen from Fig. 5A, using an optimized synthesis, it was possible to prepare catalysts with very similar phase composition.

Furthermore, Pt loading has no influence on the lattice parameters and degree of Mo incorporation characteristic for these composite materials (cf. 25BP and Pt/25BP, 25GO and Pt/25GO in Table 2). Platinum content of Pt/25B and Pt/25GO estimated by XRD analysis was in a good agreement with the 20 wt.% used in the catalysts preparation.

The influence of the mixed oxide/carbon ratios (Ti$_{0.8}$Mo$_{0.2}$O$_2$/C = 75/25, 50/50 and 25/75) in the composite supports containing BP, F-BP and Vulcan on the structure and phase composition of Pt catalysts is shown in Table 2 and Fig. 5B–D. In our previous study [57] the method of the preparation of BP- and functionalized F-BP-based composite supports for Pt electrocatalysts with 75/25 and 25/75 oxide/carbon mass ratio was already demonstrated. It has been emphasized above (see Experimental part), that the synthesis of composites with high carbon content (50C and 75C) of Mo-doped TiO$_2$ rutile structure differed from synthesis of composite materials with low carbon content (25C) in the duration and temperature of the aging step. In addition, it was necessary to compensate the whole acidity of the synthesis mixture by one more addition step of cc. HNO$_3$ before starting the aging procedure. Fig. 5B–D show, that despite of all difficulties, these problems were successfully resolved.

As seen from Fig. 5B–D and Table 2 in all BP, F-BP and Vulcan-containing samples (i) only the reflections of the TiO$_2$-rutile crystallites were present; (ii) no reflections characteristic to MoO$_2$ or MoO$_3$ oxide phase were found; (iii) the platinum was present in highly dispersed form; and (iv) no changes in the lattice parameters connected to the degree of Mo incorporation were observed (*a*=4.630 Å, *c*= 2.940 Å and Mo$_{subst}$ = 18 %).

It is necessary to mention that the less sharp diffraction peaks (see Fig. 5B–D) observed in the XRD pattern of the samples with low mixed oxide content in the carbon matrix (75C) may be attributed to the small

amount of the mixed oxide in the composite material.

3.3. Microstructure of the composite supported Pt electrocatalysts

3.3.1. N$_2$ adsorption measurements

As was mentioned above one of the main requirements for the promising electrocatalyst supports is to have a SSA not less than 100 m^2/g [2]. As can be seen from data in Table 2 (and Table S1 in the Supplementary Materials), the SSA of Ti$_{0.8}$Mo$_{0.2}$O$_2$-C composites was basically determined by two main factors (i) the mixed oxide/carbonaceous material ratio and (ii) the nature or SSA of the parent carbonaceous material. Upon decreasing the content of the carbonaceous material in the BP, functionalized F-BP and Vulcan-containing composites the SSA also decreased gradually; the lowest SSA values were obtained for the composites with Ti$_{0.8}$Mo$_{0.2}$O$_2$/C = 75/25 ratio (see 25C (C= BP, F-BP and V) samples in Table 2).

When SSA of the parent electrically conductive carbon blacks was large enough, such as for BP (S$_{BET}$= 1635 m^2/g according to Ref. [16] and 1485 m^2/g according to Ref. [70]), the presence of even 25 wt.% of carbon in the Ti$_{0.8}$Mo$_{0.2}$O$_2$-C composite materials was sufficient to get the expected SSA (see Table 2). In the case of Vulcan with much smaller SSA (S$_{BET}$= 245 m^2/g according to Ref. [16] and 232 m^2/g according to Ref. [70]), with decreasing carbon content in composites, the changes in SSA values were as follows: 175 m^2/g (75V) > 108 m^2/g (50V) > 47 m^2/g (25V). However, although the 25V composite has the lowest SSA, the surface area of this composite is still higher than that can be achieved for carbon-free mixed oxides.

Electrically conductive carbon blacks, consisting of nearly spherical primary particles fused together in aggregates, like BP have usually high SSA, but contain a significant volume of micropores, too [16]. However, it should be noted that one of the important requirements for the implementation in PEM fuel cells is an appropriate porosity of the support material in order to facilitate mass transfer of liquid fuels or oxygen gas and to minimize water flooding in electrodes [2]; in this

regard, the presence of micropores in BP carbon has negative influence on the performance of the electrocatalysts.

Both total pore volumes (Table 2) and micropore volumes (Table S1 in the Supplementary Materials) decreased parallel with the decrease of the carbon content of the $Ti_{0.8}Mo_{0.2}O_2$-C composites. This trend was valid for composites containing Vulcan, unmodified and functionalized BP carbon and was in good agreement with literature results obtained on TiO_2-coated activated carbon materials [71,72]. In this series of experiments (see Table S1 in the Supplementary Materials) the 25V composite has the smallest total pore volume (0.14 cm^3/g) and practically no micropores (<0.01 cm^3/g).

A comparison of samples with the same mixed oxide/carbon ratio (cf. 25F-BP and 25BP; 75F-BP and 75BP samples in Table 2) showed that both SSA and the pore volume were smaller on the functionalized F-BP-based composite in comparison to the unmodified BP-based ones. This may also indicate that a more uniform mixed oxide layer was formed on the functionalized carbon than on the unmodified one. Tentatively, it can be assumed that mixed oxide particles tend to block micropores of the carbonaceous material. Then a uniform coating would result in complete loss of the surface area within the pores for nitrogen adsorption. On the contrary, if only a few large grains of the mixed oxide were formed, the measured surface area should even increase somewhat, corresponding to the additive contribution of the separated species.

The shape of the isotherms obtained by nitrogen adsorption measurements also significantly depended on both the nature of the carbonaceous material and the mixed oxide/carbon ratio (see Fig. S1 in Supplementary Materials). Unmodified BP- and functionalized F-BP-based composites with 75 wt. % of carbonaceous content showed typical H1 type of hysteresis loop according the UPAC classification [73] (see Fig. S1 in the Supplementary Material). Upon increasing the mixed oxide content, the hysteresis loop became very narrow which indicates space amongst the aggregated particles rather than a well-defined cylindrical pore structure. The narrow hysteresis loop was also characteristic for all Vulcan-based samples. Contrary, isotherm of 25GO sample had a hysteresis loop of a typical H3 shape (see Fig. S1 in Supplementary Materials), which referred to the presence of aggregated flat particles and reflects the structure of the parent carbonaceous material, *i.e.* the graphene-oxide sheets of the delaminated GO.

In summary, all composite had a sufficiently large specific surface area to be used as a support for electrocatalysts in PEM fuel cells with the exception of the sample 25V as it has been mentioned in Chapter 3.1.

3.3.2. XPS investigations

Similarly to the phase composition, the general qualitative electron spectroscopic features of the composite materials and the related electrocatalysts were rather similar, irrespectively to the type of the carbon material or the mixed oxide/carbon ratio. The carbon content of all studied samples was predominantly graphitic (main C 1s peak at 284.4 eV binding energy). Only the graphite oxide-derived materials contained oxidized species in a somewhat larger amount (a small peak slightly above 286 eV arose from carbon atoms singly bound to oxygen, like in C—OH or in C—O—C in epoxide or lactone groups and another one around 288.5 eV appeared due to highly oxidized carbon species (carboxylic or anhydride functionalities [74,75]). This indicates that the steps applied during composite synthesis largely reduced even the graphite oxide. The narrow and sharp Ti $2p_{3/2}$ peak at 458.8 eV confirmed the exclusive presence of Ti^{4+} in the composite materials. The Mo 3d spectra of all samples showed the characteristics of Mo in the mixed oxide – carbon composite material as described in our previous works [45,46]. Based on XRD and XPS results no Mo-carbide formation was observed in any of our $Ti_{0.8}Mo_{0.2}O_2$ - C composite support materials due to the relatively low temperature of HTT compared to the commonly used carbide production methods [76]. The general appearance of the Mo 3d spectra were rather similar in all samples, regardless to the type of the carbonaceous material, the mixed oxide/carbon ratio or the Pt loading in the electrocatalysts (as a representative example, spectra for the mixed oxide-rich 25BP, 25V and 25GO composites are shown in Fig. S2 in Supplementary Materials). Shortly, the Mo 3d spin-orbit splitted doublet was in all cases slightly asymmetric towards the low binding energies; its main contribution arose from the Mo^{6+} ionic state (Mo $3d_{5/2}$ peak around 232.5 eV [77]), which was accompanied by weaker (around 10–20 %) Mo^{5+} ($3d_{5/2}$ peak around 231 eV [77]) and Mo^{4+} (leading peak around 230 eV [77,78]) contributions. The O 1s spectrum in all cases consisted of a strong leading peak slightly above 530 eV binding energy (arising from O ions bound to metal (Ti- or Mo) cations), which was accompanied by a tail region towards high binding energies containing contributions from hydroxyl groups on the mixed oxide and C—O—C groups in epoxide from the carbon backbone (around 531 eV) and hydroxyl and carboxyl groups on the carbon backbone along with adsorbed water (around 533 eV) [74,75]. The platinum content in all electrocatalyst was predominantly metallic (Pt $4f_{7/2}$ peak slightly above 71 eV binding energy).

In spite of the general similarity of the carbon, titanium, molybdenum or platinum chemical states in the studied samples, notable

Table 3
Composition of the mixed oxide composite supports and the studied electrocatalysts from XPS measurements.

Sample	Ti/Mo[a] (at%/at%)		Ti + Mo + O)/C (wt%/wt%)	Pt[b] (wt%)	
	XPS	ICP		XPS	ICP
25BP	2.5/1	–	58.4/41.6	–	–
50BP	2.9/1	–	46.2/53.8	–	–
75BP	3.3/1	–	22.7/77.3	–	–
25V	1.9/1	–	70.0/30.0	–	–
25V[c]	3.8/1	–	58.0/42.0	–	–
25GO	1.6/1	–	60.1/39.9	–	–
Pt/25BP	3.5/1	5.2/1 (5.0/1)[d]	58.0/42.0[e]	44.0	18.5 (22.2)[d]
Pt/50BP	3.8/1	4.7/1	40.3/59.7[e]	35.6	18.7
Pt/75BP	4.9/1	5.1/1	19.0/81.0[e]	22.0	16.2
Pt/25F-BP	3.6/1	5.1/1	70.0/30.0[e]	53.0	16.3
Pt/50F-BP	4.3/1	5.7/1	32.7/67.3[e]	39.1	17.7
Pt/75F-BP	5.2/1	6.0/1	20.0/80.0[e]	33.0	18.3
Pt/25V	3.8/1	5.2/1	61.9/38.1[e]	48.3	18.4
Pt/50V	3.6/1	5.0/1	37.2/62.8[e]	42.5	18.8
Pt/75V	4.1/1	5.7/1	19.1/80.9[e]	41.5	17.2
Pt/25GO	2.4/1	n.d.	54.8/45.2[e]	39.1	n.d.

[a] Nominal Ti/Mo= 4:1.
[b] The nominal Pt content: 20 wt.%.
[c] "Blank Pt-loading experiment": all steps of Pt loading were performed without addition of Pt precursor.
[d] Data in brackets were obtained by X-ray fluorescence (XRF) and energy dispersive X-ray spectroscopy (EDX).
[e] Calculated without the Pt content; n.d.= no data.

quantitative differences were observed between even electrocatalysts with similar nominal composition. From the evaluation of the compositional data, quantities such as the Ti/Mo ratio, weight percentage of the mixed oxide and the carbonaceous material as well as the Pt content were derived and summarized in Table 3.

As the composition calculations were based on the assumption of homogeneous distribution of the sample constituents, deviations from the nominal values reflect mainly structural deviations from the homogeneous case and differences between the samples suggest structural variations. Nevertheless, because of the complex relation between the photoelectron intensities and the sample structure, XPS is an indirect structure-sensitive tool at most, so structural considerations based on XPS data always have to be placed into context using results of direct structure determination techniques.

A general observation is that XPS detects more carbon in all samples than the nominal carbon content. The deviation is usually higher for samples with high mixed oxide content and gets smaller as the carbon content is increased. For example, according to our previous results, an apparent carbon content around 40 wt.% is typical for mixed oxide composites with a 75:25 nominal oxide/carbon weight ratio on BP carbon [46,48]. Similarly, high apparent carbon content was found in the 25GO sample. The reason for the high apparent carbon content is that the structure deviates from the homogeneous mixture of the components: the surface specific XPS technique tends to underestimate the mixed oxide content if a certain fraction is present in the form of crystallites thicker than the information depth of the method (around 10 nm), especially if the regions covered by thick mixed oxide coexist with partly or completely uncovered carbon patches (see also the TEM results in Section 3.3.3). Data in Table 3 suggest that in this sense the homogeneity of the samples increases as the amount of the carbonaceous material is increased. It is interesting to see that addition of Pt always results in further increase of the apparent relative surface carbon content, which may be interpreted by a combination of the shadowing of the mixed oxide by the deposited Pt and some mixed oxide loss during Pt loading.

Another general feature of the composites is that the Mo content deduced from the XPS measurements is always higher than the nominal value. It indicates that Mo tends to be a surface species [46,48]. In particular, the Ti/Mo ratio of the 25V or the 25GO composites is unusually low (the apparent Mo content is unusually high), which suggests segregation of Mo oxides to the surface of the support material. The tendency is again that the amount of excess Mo decreases as the carbon content increases. This is in line with the observations of the preliminary experiments which suggested better Mo incorporation for samples with higher surface area (Section 3.1). Data on the Pt-loaded electrocatalysts show Ti/Mo ratios closer to the nominal value, which is mostly due to dissolution of weakly bound surface Mo species during Pt deposition as evidenced in a blank experiment, although the shadowing effect of Pt (i. e. Mo is no longer at the outermost surface of the catalyst grains) also plays a role.

Similarly, the Pt content determined by XPS is generally well above the nominal value, which indicates that Pt is a well-dispersed surface species deposited onto the composite support. Nevertheless, the differences between the apparent Pt content of the samples on different supports are probably connected to structural differences. Comparison of data in Tables 2 and 3 of the manuscript suggest that such a structural difference could be the different specific surface area. Indeed, shadowing of the support by the Pt nanoparticles may be more important for samples with smaller surface area, resulting in higher apparent Pt content, even if the actual dispersion (particle size) of Pt is unchanged. In addition, the decrease of the apparent Pt surface excess in parallel with the increasing nominal carbon content again suggests the more homogeneous nature of the samples containing more carbonaceous material.

While the surface sensitive XPS measurements revealed notable variations among the apparent composition of the samples, less structure-sensitive methods such as ICP, XRF or EDX gave Ti/Mo ratios

or Pt content data consistent with the nominal values. This confirms that the variation of the XPS results is indeed due to structural reasons. In particular, in case of the samples with the highest carbon content, the results of the XPS and the bulk-sensitive measurements are rather close to each other, pointing again to the relative homogeneity of these materials. Accordingly, with increasing amount of carbon material it is highly probable that, as hard template, carbon can facilitate even distribution of the mixed oxide. Actually, high surface area mixed oxide "layer" or high surface area mixed oxide particles deposited in the carbonaceous backbone can be envisaged, on which Pt particles grow also in a homogeneous distribution.

3.3.3. TEM measurements

TEM images of the electrocatalysts prepared using different carbonaceous materials with various $Ti_{0.8}Mo_{0.2}O_2/C$ ratios are presented in Figs. 6–8. The appearance of well dispersed, uniformly distributed Pt on the surface of all catalysts studied was evidenced (see Figs. 6–8) consistent with XRD results (Fig. 5). The Pt particle size values determined from TEM experiments are given in Table 2. As emerges from these data the applied reduction-precipitation method led to fine dispersion of the Pt nanoparticles, which is particularly desirable for an efficient electrocatalyst. It is necessary to mention that within the experimental error, the type of the used carbonaceous materials practically did not affect the average Pt particle size.

The presence of the Pt nanoparticles with mean particle size of about 2.4 nm and narrow distribution ($\pm$ 0.9 nm) was observed for the Pt/25GO catalyst by TEM at different magnifications (Fig. 6A–C). As shown in Fig. 6A TEM measurements of this sample indicated a film-like material with varying thicknesses. The "waviness" of the particles was clearly corresponding to the presence of the reduced GO (Fig. 6A). Near the edges of the composite particle, the creased (typical for thermally degraded GO) carbon phase was also noticeable. The mixed oxide probably appeared in several morphologies, with smaller particles and larger coating-like parts; Moiré effect arising from overlapping mixed oxide crystallites in the composite materials could also be observed (Fig. 6B–C). Pt appeared in this sample in a highly dispersed form, but it was not completely evenly distributed in the composite nanoparticles (Fig. 6C).

Regarding the TEM image of the Vulcan-containing Pt/25V and Pt/50V samples, the mixed oxide morphology was inhomogeneous (Fig. 7A and B): it appeared as small particles and larger needle-like agglomeration of the rutile crystallites. Characteristic Moiré pattern could also be observed mainly on the needle-like crystallites (Fig. 7A and insert in Fig. 7B), which was consistent with high mixed oxide content of the samples and the relatively low specific surface area of the starting carbonaceous materials (see Table 2). The inhomogeneity revealed by TEM is in good agreement with the conclusions obtained from the composition data measured by XPS. Among the Vulcan-based composite supported catalysts the Pt/75V sample with the largest carbon content (Fig. 7C) had the most homogeneous structure of mixed oxide. Although needle-like formations also appeared on its TEM images, the size of those was somewhat smaller than that appeared on the samples with higher mixed oxide content and they were not dominant (Fig. 7C). The onion-like structure of the carbon material could be well recognized (insert in Fig. 7C). In these catalysts Pt was present in the form of highly dispersed spherical nanoparticles with a relatively uniform distribution; but in the Pt/25V and Pt/50V samples Pt NPs decorating only the edges of the composite particles were also detected (Fig. 7A and B).

TEM images of the Pt electrocatalysts with various $Ti_{0.8}Mo_{0.2}O_2/C$ ratios prepared using BP and F-BP carbons are presented in Fig. 8 top and bottom, respectively. Fig. 8 demonstrated that

(i) taking into account the spatial distribution of oxide crystallites in these samples, a fairly uniform oxide coating was proposed;

(ii) a more homogeneous mixed oxide structure was observed in case of the functionalized F-BP-based support (Fig. 8, bottom);
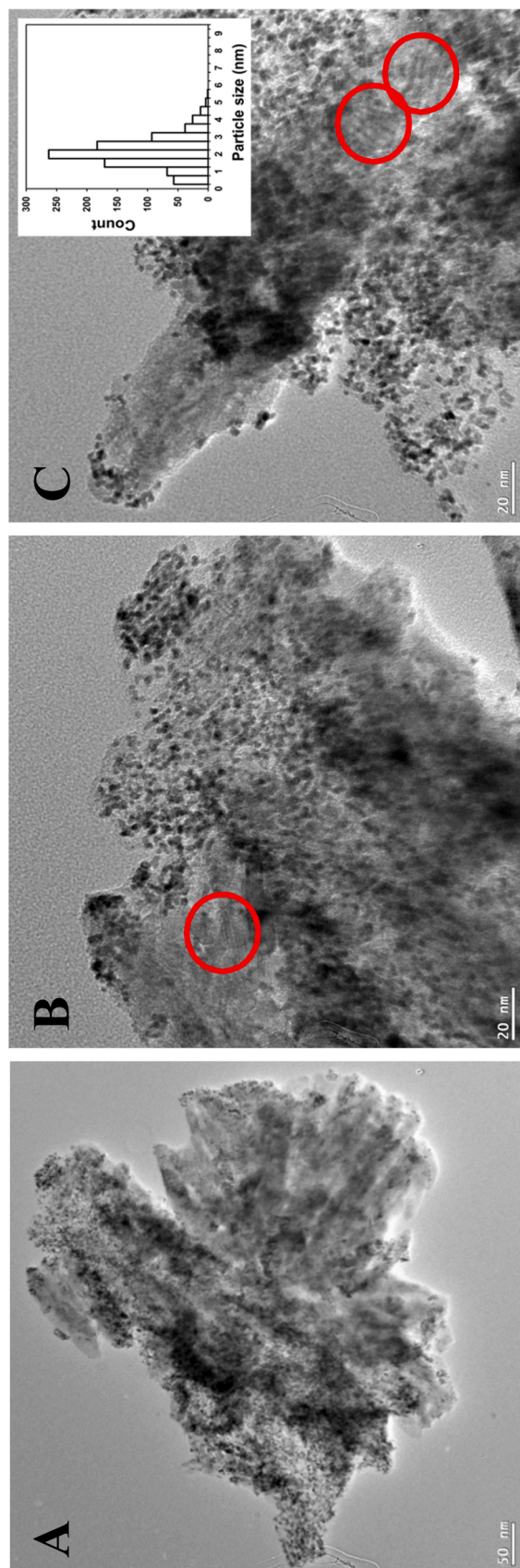
Fig. 6. TEM images and corresponding histogram of particle size distribution at lower (A) and higher magnification (B, C) for the Pt/25GO catalyst showing different mixed oxide morphologies; characteristic Moiré pattern was marked with red circle. (For interpretation of the references to colour in this figure legend, the reader is referred to the web version of this article).
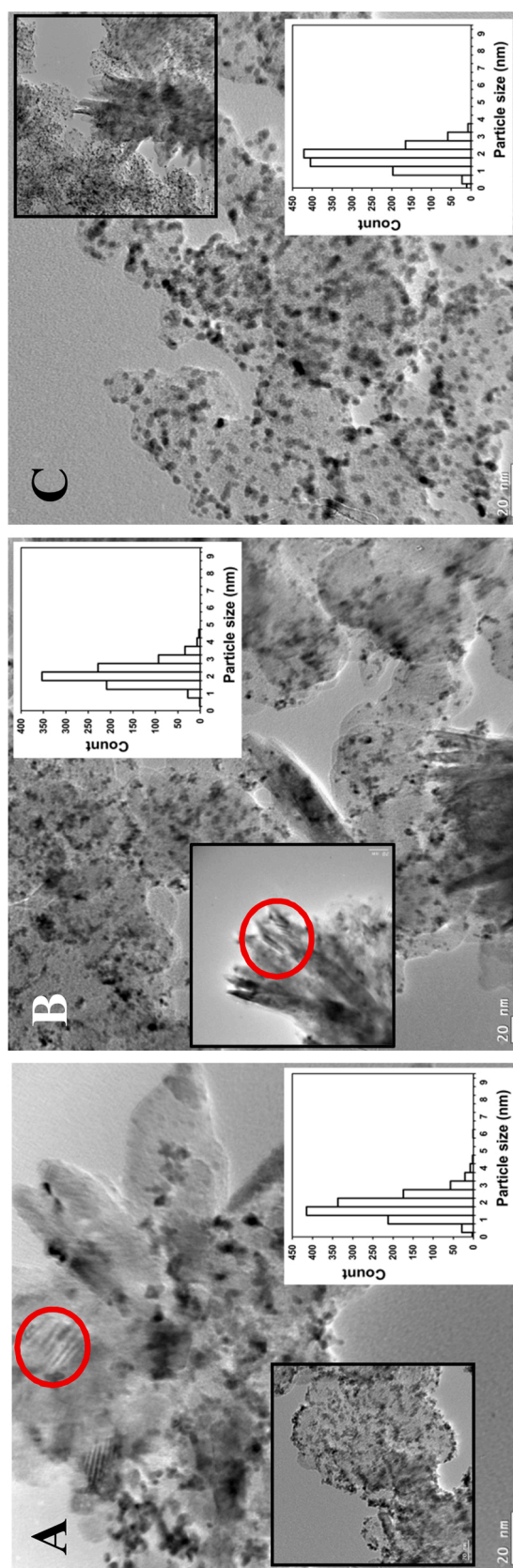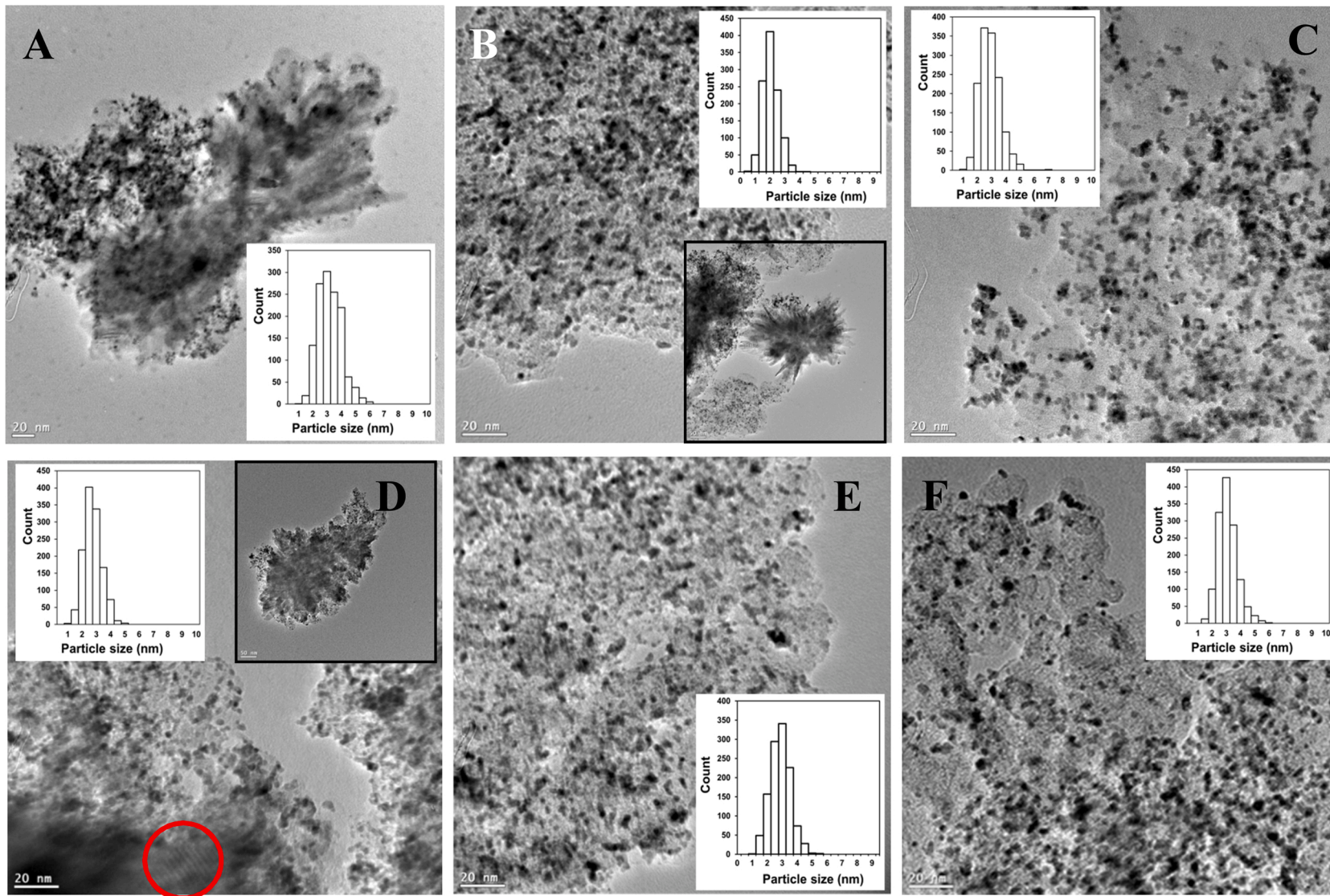

Fig. 7. TEM images and corresponding histograms of particle size distribution for the Pt/25V (A), Pt/50V (B) and Pt/75V (C) catalysts; characteristic Moiré pattern was marked with red circle. (For interpretation of the references to colour in this figure legend, the reader is referred to the web version of this article).

Fig. 8. TEM images and corresponding histograms of particle size distribution for the Pt/25BP (A), Pt/50BP (B) and Pt/75BP (C) catalysts on the top and for the Pt/25F-BP (D), Pt/50F-BP (E) and Pt/75F-BP (F) on the bottom; characteristic Moiré pattern was marked with red circle. (For interpretation of the references to colour in this figure legend, the reader is referred to the web version of this article).

(iii) quite big difference was observed between TEM images of composite materials with high (Fig. 8A and D) and low mixed oxide content (Fig. 8C and F);

(iv) the presence of a few large, faceted nanorod-like mixed oxide rutile crystallites decorated with Pt was more typical for the unmodified BP-based composites with high mixed oxide content (Fig. 8A and B); in case of the F-BP-based composites these large, rutile crystallites were observed only in the Pt/25F-BP catalysts (Fig. 8D, insert);

(v) in the samples with high content of carbonaceous materials (Fig. 8C and F) the presence of the oxide layers over carbon was less obvious, pointing to a more homogeneous system as suggested by the XPS results;

(vi) the presence of the Moiré pattern was more characteristic for the composites with high mixed oxide content (Fig. 8A and D).

The TEM results presented here are in good agreement with our previous observations obtained on the Mo-containing composite materials, demonstrating that the functionalization of carbon modifies in some extent the nucleation and growth of the rutile-TiO_2 phase on carbon materials, which may have some beneficial effect on mixed oxide coating of the carbonaceous backbone [57].

3.4. Electrochemical characterisation

The preliminary results demonstrated the importance of the exclusive presence of the rutile phase of the Mo-doped TiO_2 on the electrochemical properties of the $Ti_{0.8}Mo_{0.2}O_2$-C composite supported electrocatalysts. The influence of the mixed oxide/carbon ratios ($Ti_{0.8}Mo_{0.2}O_2$/C = 75/25, 50/50 and 25/75) in the F-BP-, BP- and Vulcan-based composite supports on the electrochemical performance of the catalysts was visualized in Fig. 9 and in Figs. S3 and S4 of the Supplementary Material.

The performance of all electrocatalysts was studied by cyclic voltammetry, CO_{ads}-stripping voltammetry measurements done before and

Table 4
Electrochemical performance of the $Ti_{0.8}Mo_{0.2}O_2$-C composite supported 20 wt. % Pt electrocatalysts.

Sample	$E_{CO,max}$,[a] mV	$ECSA_1$, m^2/g_{Pt}	$\Delta ECSA_{500}$, %[b,c]	$\Delta ECSA_{10,000}$, %[b]
Pt/25BP	705 (*sh*: 745)	81.6	7.4	37.0
Pt/50BP	705 (*sh*: 745)	79.2	8.6	34.1
Pt/75BP	775	69.1	11.8	27.6
Pt/25F-BP	705 (*sh*: 745)	60.9	7.0	30.5
Pt/50F-BP	705 (*sh*: 745)	67.6	7.3	31.2
Pt/75F-BP	775	65.4	11.2	24.1
Pt/25V	705 (*sh*: 745)	81.3	9.0	43.6
Pt/50V	705 (*sh*: 745)	73.0	10.1	35.0
Pt/75V	755	83.0	12.2	36.4
Pt/25GO	705 (*sh*: 745)	77.6	8.4	36.0
Pt/C	795	94.5	12.7	47.8

[a] The position of the main CO stripping peak measured on fresh catalysts; ***sh*** = shoulder.

[b] $\Delta ECSA_{500}$ and $\Delta ECSA_{10,000}$ were calculated from the charges originated from the hydrogen desorption in the 1st and 500th or 10,000th cycles according to the Eq. 1 (see Experimental part).

[c] $\Delta ECSA_{500}$ values were calculated from the present 10,000-cycle stability measurements.

after the 500-cycle stability test, as well as by the electrochemical long-term stability test involving 10,000 polarization cycles (see Table 4 and Figs. 9, S3 and S4).

As it was mentioned above the synthesis procedure of $Ti_{0.8}Mo_{0.2}O_2$–C composite materials with different $Ti_{0.8}Mo_{0.2}O_2$/C ratios was optimized for preparation of the F-BP-, BP- and Vulcan-based supports with almost
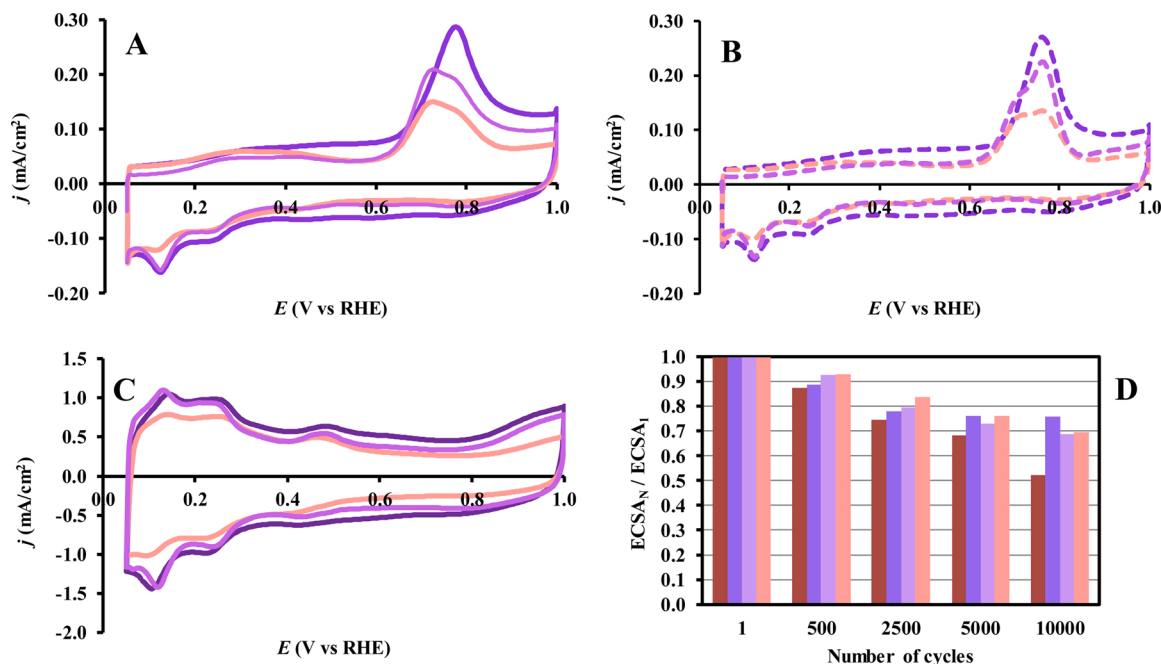

Fig. 9. Influence of the $Ti_{0.8}Mo_{0.2}O_2$/C ratios in functionalized F-BP-based composite materials on the electrochemical performance of the catalysts. CO_{ads}-stripping voltammograms of the electrocatalysts obtained before (A) and after the 500-cycle stability test (B). Cyclic voltammograms of the fresh BP-based electrocatalysts (C) and the results of the electrochemical long-term stability test (D): comparison of the electrochemically active Pt surface area measured after N cycles normalized to ECSA measured in the 1st cycle ($ECSA_N$/$ECSA_1$) of the Pt/25F-BP ( ), Pt/50F-BP ( ) and Pt/75F-BP ( ) catalysts as a function of the number of cycles (N); results obtained on the 20 wt.% reference Pt/C catalyst ( ) is given for comparison. Recorded in 0.5 M H_2SO_4 at 10 mV/s (A, B) and 100 mV/s (C), T=25 °C.

complete incorporation of the Mo into the rutile-TiO_2 lattice. However, according to the XPS, TEM and nitrogen adsorption measurements results quite big difference was observed in the microstructure of the composites and the related Pt electrocatalysts with different mixed oxide/carbon ratios (see Table 2).

As seen from Figs. 9A, S3.A and S4.A on all F-BP-, BP- and Vulcan-containing Pt catalysts the CO electrooxidation ("pre-peak") started at exceptionally low potential values ($E_{CO,onset}$=50 mV). According to the literature [79,80] and our previous studies [45,49] the so-called "pre-peak" consists of at least two oxidation reactions: partial oxidation of weakly adsorbed CO on specific Pt sites, where Pt and Mo atoms are in atomic closeness, and oxidation of Mo surface species.

The position of the maximum of the main CO oxidation peak observed on the CO_{ads}-stripping curves for various $Pt/Ti_{0.8}Mo_{0.2}O_2$–C electrocatalysts is summarized in Table 4. On the unmodified and functionalized BP-containing composite supported catalyst with high carbon content (Pt/75C) the main CO_{ads}-stripping peak (oxidation of strongly bonded CO) was located at ca. 775 mV, while in the case of the catalysts with lower carbon content (Pt/25C and Pt/50C) two overlapping CO_{ads}-electrooxidation peaks at less positive potentials (around 705 and 745 mV) were observed (see Figs. 9A and S3.A). Thus, an increase of the mixed oxide content in the composite materials resulted in the increase of the CO tolerance of the catalysts. It should be noted that in the case of the reference Pt/C catalyst, the corresponding peak was at about 795 mV (see Table 4).

After 500 cycles of the stability test (Figs. 9B and S3.B) the main CO stripping peak on the catalysts with high carbon content (Pt/75C) shifted ca. 10 mV toward less positive potential values in comparison to that obtained over fresh samples. This kind of shift can be an indication of the agglomeration of Pt nanoparticles [81]. In case of Vulcan-containing catalysts (see Fig. S4.A and B) the only difference was observed in the position of the main anodic peak of the Pt/75V catalyst, which was located at about 755 mV (Table 4).

In Ref. [82] the presence of two electrooxidation peaks was ascribed to the CO oxidation on Pt nanoparticles with different structures (e.g., due to the agglomeration of Pt nanoparticles and formation of nano-grained structures with high surface defect density). However, the position of the CO_{ads} electrooxidation peaks can also be considered from the viewpoint of the degree of the interaction between the Pt nanoparticles and Mo-containing composite support. Based on the literature [82] and our own results [45,46,48] it has been proposed that better CO tolerance can be achieved on Pt sites at the interface with Mo-modified TiO_2-C composite, when the interaction between Pt and Mo is maximized (Pt nanoparticles perfectly distributed over the mixed oxide coating, without any contact with carbon). In this respect the peak at 775 mV observed on the BP- and F-BP-containing catalysts can be attributed to CO_{ads} electrooxidation on Pt nanoparticles with a less pronounced effect of Mo-modified composite materials; in contrast, the shift of this peak on the Pt/75V catalyst ~ 20 mV toward less positive potential values (see Table 4) may indicate better mixed oxide coating over carbon.

As it was mentioned above the presence of well dispersed, uniformly distributed Pt on the surface of the all catalysts studied was evidenced by TEM (see Figs. 6–8). However, a rather big difference was observed between the TEM images of catalysts with high and low contents of mixed oxides: Pt appeared in all catalysts in a highly dispersed form, but in a different environment. Depending on the mixed oxide/carbon ratio, Pt nanoparticles deposited only on small composite particles or on small and larger needle- or nanorod-like clusters of rutile crystallites were observed.

According to these findings the presence of one main electrooxidation peak on the catalysts with low mixed oxide content in composite supports (Pt/75C) can be explained by the most homogeneous structure of the mixed oxide (lacking big crystallites); an exception is the Pt/75V catalyst, in which the presence of needle-like crystallites was demonstrated by TEM (see Fig. 7C).

A typical cyclic voltammogram (CV) of Pt with the classical features of the adsorption/desorption of underpotentially deposited hydrogen between 50 and 350 mV along with a redox peak pair of the Mo between 380 and 530 mV was observed on the all studied catalysts (Figs. 9C, S3.C and S4.C). According to the literature and our previous observations [45,46,83,84] the appearance of these redox peaks in the voltammograms clearly confirm that there is an active interface between the Pt NPs and the surface Mo species of the composite support. A good correlation was found between the Pt particle size of the catalysts presented in Table 2 and the intensity of the hydrogen adsorption/desorption peaks found on the CVs. It is necessary to mention, that increase of the content of carbonaceous materials in the composites from 25 to 75 wt.% resulted in a pronounced increase of the double layer charging, which correlated with well with BET surface area calculated from N_2 adsorption measurements.

The electrochemically active Pt surface area (ECSA) of the electrocatalysts presented in Table 4 was calculated from the charge transfer accompanying the hydrogen desorption taking into account the capacitive currents, originated from the double layer charging of the CVs. The values of the ECSA loss (ΔECSA) as a function of the number of cycles of the stability test calculated for the reference Pt/C and F-BP-, BP- and Vulcan-containing composite supported Pt catalysts with different $Ti_{0.8}Mo_{0.2}O_2$/C ratios was presented in Table 4 and Figs. 9D, S3.D, and S4.D (for details see in Experimental part).

In Fig. 10 the loss of the ECSA after the 500-cycle and 10,000-cycle stability test was visualized for all studied catalysts. As shown in Fig. 10 after 500 polarization cycles, the catalysts with high mixed oxide content (Pt/25C) were the most stable, but the behavior of the catalysts with high carbon content (Pt/75C) was only slightly better than the stability of the reference Pt/C. However, the situation changed completely after 10,000 polarization cycles. According to the results of the 10,000-cycle stability tests the Pt/75F-BP and Pt/75BP catalysts with $Ti_{0.8}Mo_{0.2}O_2$/C ratios of 25/75 seemed to be more promising (see Table 4). Moreover, according to the TEM results among all studied catalysts the functionalized F-BP-based composite supports had the most homogeneous mixed oxide structure (see Fig. 8, bottom). As shown in Fig. 10 after 10,000 polarization cycles these F-BP-based composite supported Pt catalysts have the highest stability in comparison with the BP- and Vulcan-containing samples.

The influence of the type of carbonaceous material on the electrochemical performance of the composite supported Pt/25C (C= BP, V and GO) catalysts with low carbon content is presented in Fig. 11. However, comparison of Figs. 9 and 11 reveals that the type of the carbonaceous material in the case of the 25 wt.% carbon containing composites does not have such a noticeable effect on the electrochemical characteristics
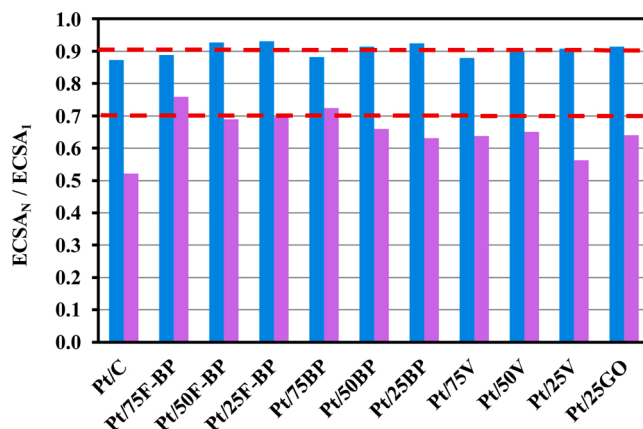

Fig. 10. Comparison of the electrochemically active Pt surface area measured after N cycles normalized to ECSA measured in the 1st cycle ($ECSA_N/ECSA_1$) of the 20 wt.% reference Pt/C and composite supported Pt catalysts as a function of the number of cycles: N = 500-cycle (■) and 10,000-cycle (■).
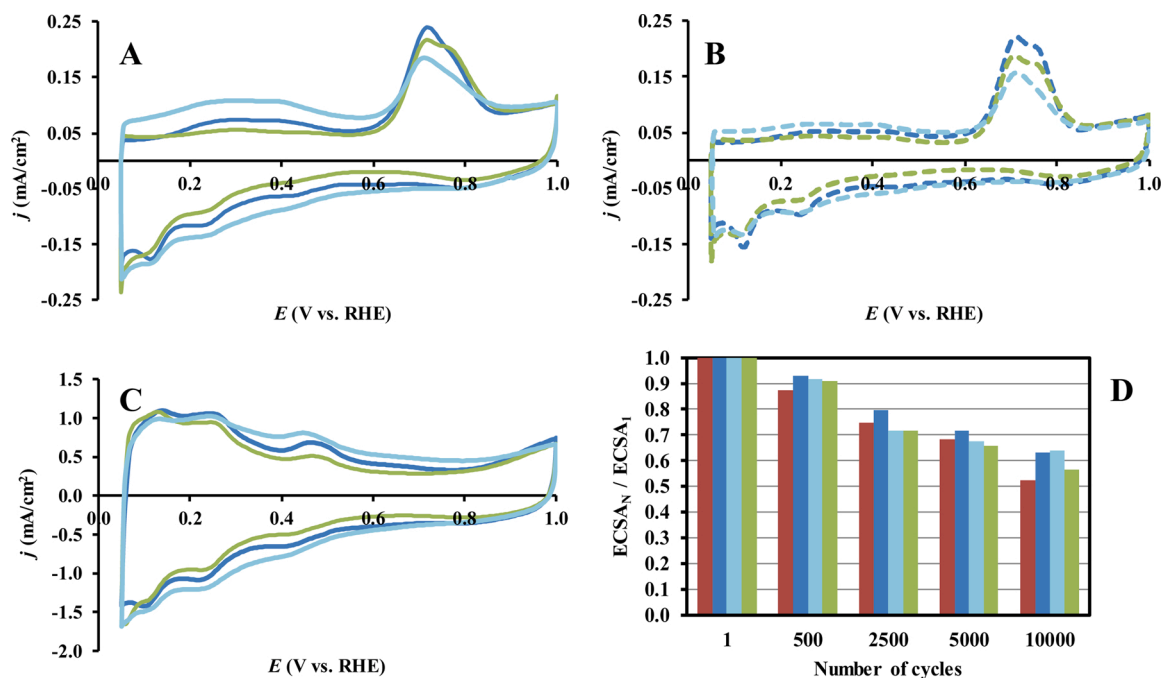
Fig. 11. Influence of the type of carbonaceous material used for the preparation of 75Ti$_{0.8}$Mo$_{0.2}$O$_2$-25C (C= BP, V and GO) composite support materials on the electrochemical performance of the corresponding Pt catalysts. CO$_{ads}$-stripping voltammograms of the electrocatalysts obtained before (A) and after the 500-cycle stability test (B). Cyclic voltammograms of the fresh 20 wt.% Pt/75Ti$_{0.8}$Mo$_{0.2}$O$_2$-25C electrocatalysts (C) and the results of the electrochemical long-term stability test (D): comparison of the electrochemically active Pt surface area measured after N cycles normalized to ECSA measured in the 1st cycle (ECSA$_N$/ECSA$_1$) of the Pt/25BP (■), Pt/25GO (■) and Pt/25V (■) catalysts as a function of the number of cycles (N); results obtained on the 20 wt.% reference Pt/C catalyst (■) is given for comparison. Recorded in 0.5 M H$_2$SO$_4$ at 10 mV/s (A, B) and 100 mV·s^{-1} (C), T=25 °C.

as the Ti$_{0.8}$Mo$_{0.2}$O$_2$/C ratio.

As shown in Fig. 11A the main difference observed in the CO$_{ads}$ stripping voltammograms of these catalysts was the intensity of the "pre-peak" area: it was quite pronounced for the Pt/25GO catalyst. According to the histogram of particle size distribution (see insert in Fig. 6C) very small Pt nanoparticles (below 1 nm) were also present in Pt/25GO catalyst. Other investigated catalysts did not contain particles below 1 nm in such an amount. However, after 500 polarization cycles, this difference disappeared (see Fig. 11B).

We demonstrated earlier [50] that after 500-cycle stability test done on the Pt/25BP catalysts a certain small increase of the main Pt particle size from 3.0 ± 0.8 nm to 4.2 ± 1.9 nm was observed. Apparently, sintering primarily affects the smallest Pt particles.

As was mentioned above, two overlapping CO$_{ads}$-electrooxidation peaks at around 705 and 745 mV were observed on the BP- and Vulcan-containing Pt/25C catalysts (see Table 4). As shown in Fig. 11A in the case of the Pt/25GO catalyst, the presence of a shoulder at about 745 mV was not so obvious. This difference in the shape of the CO$_{ads}$-stripping voltammograms of the Pt/25C catalysts persisted after 500-cycle stability test (see Fig. 11B).

The cyclic voltammogram of the fresh Pt/25GO electrocatalyst (see Fig. 11C) was very similar to that obtained on Pt/25C catalysts containing BP and Vulcan. It is necessary to mention, that among the catalysts presented in Table 2 these three catalysts have the lowest SSA, which is reflected in the low charge of the double layer.

As shown in Figs. 10 and 11D the stability of these catalysts after 500 polarization cycles was high and quite similar. However, as it has already been mentioned, the catalysts with high mixed oxide content showed the highest degradation after the 10,000-cycle stability test; the loss in the electrochemical surface area (ΔECSA) increased in the following order: Pt/25GO ≈ Pt/25BP < Pt/25 V (see Table 4). The heterogeneity of the mixed oxide structure observed by XPS and TEM for the Pt/25C catalysts can be a reason of the lower stability comparing to the more homogeneous Pt/75C samples. In case of such a heterogeneous

system, especially with low surface area, Pt particles can occur in many different environments ranging from carbonaceous patches hardly covered by mixed oxide through segregated Mo-oxide regions to areas with stable mixed oxide formations. Pt not coupled to mixed oxide or interacting with segregated Mo-oxides is known to suffer from strong degradation under potential cycling due to electrocorrosion or Mo dissolution potentially leading even to detachment of the Pt particles. A clear example for this kind of instability is given in Fig. 3, where in the case of the very inhomogeneous Pt/25F-V catalyst the CO$_{ads}$-stripping voltammogram suggests the complete loss of Pt not strongly coupled to the mixed oxide during the potential cycling test. On the other hand, the more homogeneous distribution of Mo in the rutile matrix experienced in case of the Pt/75C catalysts, which prevents dissolution of Mo, may provide a good anchoring option for Pt on the mixed oxide.

The electrochemical results indicate that there are characteristic performance differences between the electrocatalysts with different mixed oxide/carbon ratio. It is not surprising that the Mo-Pt interactions are more pronounced if the mixed oxide content is increased, so better initial CO-tolerant properties are observed in the Pt/25C or Pt/50C type materials than in the Pt/75C ones, which advantage completely disappears in long term stability tests. Even after 500 cycles the ratio of pre-peak to main CO oxidation peak become similar in each sample, irrespectively the catalytic materials. Moreover, the more homogeneous microstructure of the Pt/75C catalysts seems to be the key for enhanced stability. Considering also the fact that high oxide content in the catalyst layer can lead to a slight increase of the cell resistance, the Pt/75F-BP and Pt/75BP catalysts with Ti$_{0.8}$Mo$_{0.2}$O$_2$/C = 25/75 ratio seems to be more promising.

4. Conclusions

Taking into account the peculiarities of various carbonaceous materials, the synthesis procedure of the mixed oxide–carbon composite type electrocatalyst supports with different Ti$_{0.8}$Mo$_{0.2}$O$_2$/C ratios was

successfully optimized for use of Vulcan, unmodified BP and functionalized F-BP carbon materials. The multistep sol-gel-based synthesis method was also adapted to obtain GO-derived composite with 25 wt.% GO and rutile-TiO_2 structure. It was demonstrated that the time and temperature of aging and maintenance of the appropriate acidic pH during the synthesis played key role in exclusive formation of the rutile phase, which is essential for good Mo incorporation and enhanced stability. As demonstrated by XRD, almost complete incorporation of the Mo-dopant into substitutional sites of the TiO_2 lattice, which protect the doping metals from dissolution, was achieved.

According to XPS, TEM and nitrogen adsorption measurements, electrocatalysts with different microstructures can be obtained depending on the nature of the carbonaceous material and the mixed oxide/carbon ratio applied during the synthesis. With increasing carbonaceous material content in the composites, an increase in the specific surface area was observed. In the samples with high content of carbonaceous materials the carbonaceous backbone behaves as a good hard template leading to homogeneous distribution of mixed oxide particles/layers over carbon. Functionalization of carbon modified in some extent the nucleation and growth of the rutile-TiO_2 phase on carbon materials, which may have some beneficial effect on mixed oxide coating of the carbonaceous backbone. The appearance of well dispersed, uniformly distributed Pt on the surface of the all catalysts studied was evidenced by TEM; the type of used carbonaceous materials practically did not affect the average Pt particle size.

Electrochemical investigations revealed significantly improved CO-tolerance and stability for the composite supported electrocatalysts compared to the Pt/C reference system. However, characteristic performance differences were found between the catalysts with different mixed oxide/carbon ratio. As the key requirement for CO tolerance is an intimate interaction between the surface Mo species and the Pt nanoparticles, composites containing 50 or 75 wt.% mixed oxide exhibited better initial CO-tolerant behavior. However, long-term stability tests suggested improved behavior for the catalysts with higher carbon content (Pt/75C), indicating that the more homogeneous microstructure observed for these catalysts may be the key for enhanced stability. At the same time, the type of the carbonaceous material seemed to play a smaller role in determining the stability of the catalysts, although Black Pearls-based supports performed typically better. Taking into account that upon application in fuel cells the high oxide content in the catalyst layer can lead to a slight increase of the cell resistance, our results indicate that the Pt/75BP and Pt/75F-BP electrocatalysts with $Ti_{0.8}Mo_{0.2}O_2/C = 25/75$ ratio are more promising for general use.

CRediT authorship contribution statement

Irina Borbáth: Conceptualization, Methodology, Validation, Writing - original draft, Writing - review & editing. **Emília Tálas:** Methodology, Investigation, Writing - original draft. **Zoltán Pászti:** Investigation, Writing - review & editing. **Kristóf Zelenka:** Investigation. **Ilgar Ayyubov:** Investigation. **Khirdakhanim Salmanzade:** Investigation. **István E. Sajó:** Investigation. **György Sáfrán:** Investigation. **András Tompos:** Supervision, Conceptualization, Writing - review & editing, Funding acquisition.

Declaration of Competing Interest

The authors report no declarations of interest.

Acknowledgements

Appendix A. Supplementary data

Supplementary material related to this article can be found, in the online version, at doi:https://doi.org/10.1016/j.apcata.2021.118155.

References

[1] B.G. Pollet, S.S. Kocha, I. Staffell, Curr. Opin. Electrochem. 16 (2019) 90–95, https://doi.org/10.1016/j.coelec.2019.04.021.

[2] Z. Zhang, J. Liu, J. Gu, L. Su, L. Cheng, Energy Environ. Sci. 7 (2014) 2535–2558, https://doi.org/10.1039/c3ee43886d.

[3] W. Gu, R.N. Carter, P.T. Yu, H.A. Gasteiger, ECS Trans. 11 (1) (2007) 963–973, https://doi.org/10.1149/1.2781008.

[4] M.M. Mench, E.C. Kumbar, T.N. Veziroglu, Polymer Electrolyte Fuel Cell Degradation, Academic Press Elsevier, Waltham, 2012, https://doi.org/10.1016/C2010-0-67819-9.

[5] J.C. Meier, C. Galeano, I. Katsounaros, A.A. Topalov, A. Kostka, F. Schuüth, K.J. J. Mayrhofer, ACS Catal. 2 (2012) 832–843, https://doi.org/10.1021/cs300024h.

[6] M.F. Mathias, R. Makharia, H.A. Gasteiger, J.J. Conley, T.J. Fuller, C.I. Gittleman, S.S. Kocha, D.P. Miller, C.K. Mittelsteadt, T. Xie, S.G. Yan, P.T. Yu, Electrochem. Soc. Interface 14 (2005) 24–35.

[7] J. Zhao, X. Li, Energy Convers. Manage. 199 (2019) 112022, https://doi.org/10.1016/j.enconman.2019.112022.

[8] D. Wang, C.V. Subban, H. Wang, E. Rus, F.J. DiSalvo, H.D. Abruña, J. Am. Chem. Soc. 132 (2010) 10218–10220, https://doi.org/10.1021/ja102931d.

[9] T. Ioroi, T. Akita, S. Yamazaki, Z. Siroma, N. Fujiwara, K. Yasuda, Electrochim. Acta 52 (2006) 491–498, https://doi.org/10.1016/j.electacta.2006.05.030.

[10] S.Y. Huang, P. Ganesan, B.N. Popov, Appl. Catal. B: Environ. 102 (2011) 71–77, https://doi.org/10.1016/j.apcatb.2010.11.026.

[11] S.Y. Huang, P. Ganesan, B.N. Popov, J. Am. Chem. Soc. 131 (2009) 13898–13899, https://doi.org/10.1021/ja904810h.

[12] C.V. Subban, Q. Zhou, A. Hu, T.E. Moylan, F.T. Wagner, F.J. DiSalvo, J. Am. Chem. Soc. 132 (2010) 17531–17536, https://doi.org/10.1021/ja1074163.

[13] T.T. Nguyen, V.T.T. Ho, C.J. Pan, J.Y. Liu, H.L. Chou, J. Rick, W.H. Su, B.J. Hwang, Appl. Catal. B: Environ. 154-155 (2014) 183–189, https://doi.org/10.1016/j.apcatb.2014.02.018.

[14] Y. Gao, M. Hou, Z. Shao, C. Zhang, X. Qin, B. Yi, J. Energy Chem. 23 (2014) 331–337, https://doi.org/10.1016/S2095-4956(14)60155-8.

[15] A. Kumar, V. Ramani, J. Electrochem. Soc. 160 (2013) F1207–F1215, https://doi.org/10.1149/2.038311jes.

[16] D. Pantea, H. Darmstadt, S. Kaliaguine, C. Roy, Appl. Surf. Sci. 217 (2003) 181–193, https://doi.org/10.1016/S0169-4332(03)00550-6.

[17] Q. Lv, M. Yin, X. Zhao, C. Li, C. Liu, W. Xing, J. Power Sources 218 (2012) 93–99, https://doi.org/10.1016/j.jpowsour.2012.06.051.

[18] J. Huang, J. Zang, Y. Zhao, L. Dong, Y. Wang, Mater. Lett. 137 (2014) 335–338, https://doi.org/10.1016/j.matlet.2014.09.051.

[19] K. Huang, K. Sasaki, R.R. Adzic, Y. Xing, J. Mater. Chem. 22 (2012) 16824–16832, https://doi.org/10.1039/c2jm32234j.

[20] A. Zhao, J. Masa, W. Xia, Phys. Chem. Chem. Phys. 17 (2015) 10767–10773, https://doi.org/10.1039/c5cp00369e.

[21] Y. Wang, A. Tabet-Aoul, M. Mohamedi, J. Power Sources 299 (2015) 149–155, https://doi.org/10.1016/j.jpowsour.2015.08.106.

[22] X. Liu, J. Chen, G. Liu, L. Zhang, H. Zhang, B. Yi, J. Power Sources 195 (2010) 4098–4103, https://doi.org/10.1016/j.jpowsour.2010.01.077.

[23] A. Bauer, C. Song, A. Ignaszak, R. Hui, J. Zhang, L. Chevallier, D. Jones, J. Roziére, Electrochim. Acta 55 (2010) 8365–8370, https://doi.org/10.1016/j.electacta.2010.07.025.

[24] E. Antolini, Appl. Catal. B: Environ. 88 (2009) 1–24, https://doi.org/10.1016/j.apcatb.2008.09.030.

[25] M.D. Obradović, G.D. Vuković, S.I. Stevanović, V.V. Panić, P.S. Uskoković, A. Kowal, S.Lj. Gojković, J. Electroanal. Chem. 634 (2009) 22–30, https://doi.org/10.1016/j.jelechem.2009.07.001.

[26] C.K. Poh, S.H. Lim, H. Pan, J. Lin, J.Y. Lee, J. Power Sources 176 (2008) 70–75, https://doi.org/10.1016/j.jpowsour.2007.10.049.

[27] C. Odetola, L. Trevani, E.B. Easton, J. Power Sources 294 (2015) 254–263, https://doi.org/10.1016/j.jpowsour.2015.06.066.

[28] M. Hakamizadeh, S. Afshar, A. Tadjarodi, R. Khajavian, M.R. Fadaie, B. Bozorgi, Int. J. Hydrogen Energy 39 (2014) 7262–7269, https://doi.org/10.1016/j.ijhydene.2014.03.048.

[29] C. Odetola, E.B. Easton, L. Trevani, Int. J. Hydrogen Energy 41 (2016) 8199–8208, https://doi.org/10.1016/j.ijhydene.2015.10.035.

[30] N. Zhang, M. Yang, S. Liu, Y. Sun, Y.J. Xu, Chem. Rev. 115 (2015) 10307–10377, https://doi.org/10.1021/acs.chemrev.5b00267, and the references cited herein.

[31] Y. Liang, H. Wang, H.S. Casalongue, Z. Chen, H. Dai, Nano Res. 3 (2010) 701–705, https://doi.org/10.1007/s12274-010-0033-5.

[32] T. Szabó, E. Tombácz, E. Illés, I. Dékány, Carbon 44 (2006) 357–545, https://doi.org/10.1016/j.carbon.2005.08.005.

[33] A.V. Talyzin, T. Szabó, I. Dékány, F. Langenhorst, P.S. Sokolov, V.L. Solozhenko, J. Phys. Chem. C 113 (2009) 11279–11284, https://doi.org/10.1021/jp9016272.

[34] A.A. Ismail, R. Geioushy, H. Bouzid, S.A. Al-Sayari, A. Al-Hajry, D.W. Bahnemann, Appl. Catal. B: Environ. 129 (2013) 62–70, https://doi.org/10.1016/j.apcatb.2012.09.024.

[35] G. Nagaraju, K. Manjunath, S. Sarkar, E. Gunter, S.R. Teixeira, J. Dupont, Int. J. Hydrogen Energy 40 (2015) 12209–12216, https://doi.org/10.1016/j.ijhydene.2015.07.094.

[36] W. Fan, Q. Lai, Q. Zhang, Y. Wang, J. Phys. Chem. C 115 (2011) 10694–10701, https://doi.org/10.1021/jp2008804.

[37] K. Majrik, Á. Turcsányi, Z. Pászti, T. Szabó, A. Domján, J. Mihály, A. Tompos, I. Dékány, E. Tálas, Top. Catal. 61 (2018) 1323–1334, https://doi.org/10.1007/s11244-018-0989-z.

[38] X. Zhang, Q. Liu, X. Shi, A.M. Asiri, Y. Luo, X.S.T. Li, J. Mater. Chem. A 6 (2018) 17303–17306, https://doi.org/10.1039/c8ta05627g.

[39] W. Zhuang, L. He, J. Zhu, R. An, X. Wu, L. Mu, X. Lu, L. Lu, X. Liu, H. Ying, Int. J. Hydrogen Energy 40 (2015) 3679–3688, https://doi.org/10.1016/j.ijhydene.2015.01.042.

[40] H. Zhang, X. Han, Y. Zhao, J. Electroanal. Chem. 799 (2017) 84–91, https://doi.org/10.1039/C3TA13155F.

[41] M. Wang, Z. Wang, L. Wei, J. Li, X. Zhao, M. Wang, Z. Wang, L. Wei, J. Li, X. Zhao, Chin. J. Catal. 38 (2017) 1680–1687, https://doi.org/10.1016/S1872-2067(17)62876-6.

[42] L. Zhao, Z.-B. Wang, J. Liu, J.-J. Zhang, X.-L. Sui, L.-M. Zhang, D.-M. Gu, J. Power Sources 279 (2015) 210–217, https://doi.org/10.1016/j.jpowsour.2015.01.023.

[43] N. Royaei, T. Shahrabi, Y. Yaghoubinezhad, Catal. Sci. Technol. 8 (2018) 4957–4974, https://doi.org/10.1039/c8cy01353e.

[44] D. Gubán, I. Borbáth, Z. Pászti, I. Sajó, E. Drotár, M. Hegedűs, A. Tompos, Appl. Catal. B: Environ. 174 (2015) 455–470, https://doi.org/10.1016/j.apcatb.2015.03.031.

[45] Á. Vass, I. Borbáth, I. Bakos, Z. Pászti, I.E. Sajó, A. Tompos, Top. Catal. 61 (2018) 1300–1312, https://doi.org/10.1007/s11244-018-0988-0.

[46] D. Diczházi, I. Borbáth, I. Bakos, G.P. Szijjártó, A. Tompos, Z. Pászti, Catal. Today (2020), https://doi.org/10.1016/j.cattod.2020.04.004.

[47] D. Gubán, Z. Pászti, I. Borbáth, I. Bakos, E. Drotár, I. Sajó, A. Tompos, Period. Polytech.-Chem. 60 (2016) 29–39, https://doi.org/10.3311/PPch.8227.

[48] Á. Vass, I. Borbáth, Z. Pászti, I. Bakos, I.E. Sajó, P. Németh, A. Tompos, React. Kinet. Mech. Catal. 121 (2017) 141–160, https://doi.org/10.1007/s11144-017-1155-5.

[49] I. Bakos, I. Borbáth, Á. Vass, Z. Pászti, A. Tompos, Top. Catal. 61 (2018) 1385–1395, https://doi.org/10.1007/s11244-018-1035-x.

[50] Á. Vass, I. Borbáth, I. Bakos, Z. Pászti, G. Sáfrán, A. Tompos, React. Kinet. Mech. Catal. 126 (2019) 679–699, https://doi.org/10.1007/s11144-018-1512-z.

[51] D. Gubán, A. Tompos, I. Bakos, Á. Vass, Z. Pászti, E.Gy. Szabó, I.E. Sajó, I. Borbáth, Int. J. Hydrogen Energy 42 (2017) 13741–13753, https://doi.org/10.1016/j.ijhydene.2017.03.080.

[52] M.S. Yazici, S. Dursun, I. Borbáth, A. Tompos, Int. J. Hydrogen Energy (2020), https://doi.org/10.1016/j.ijhydene.2020.08.226.

[53] S. von Kraemer, K. Wikander, G. Lindbergh, A. Lundblad, A.E.C. Palmqvist, J. Power Sources 180 (2008) 185–190, https://doi.org/10.1016/j.jpowsour.2008.02.023.

[54] A.B. Kuriganova, I.N. Leontyev, A.S. Alexandrin, O.A. Maslova, A.I. Rakhmatullin, N.V. Smirnova, Mendeleev Commun. 27 (2017) 67–69, https://doi.org/10.1016/j.mencom.2017.01.021.

[55] Z.Z. Jiang, D.M. Gu, Z.B. Wang, W.L. Qu, G.P. Yin, K.J. Qian, J. Power Sources 196 (2011) 8207–8215, https://doi.org/10.1016/j.jpowsour.2011.05.063.

[56] Y.J. Wang, D.P. Wilkinson, V. Neburchilov, C. Song, A. Guest, J. Zhang, J. Mater. Chem. A 2 (2014) 12681–12685, https://doi.org/10.1039/c4ta02062f.

[57] I. Borbáth, K. Zelenka, Á. Vass, Z. Pászti, G.P. Szijjártó, Z. Sebestyén, G. Sáfrán, A. Tompos, Int. J. Hydrogen Energy (2020), https://doi.org/10.1016/j.ijhydene.2020.08.002.

[58] G.S. Pawley, J. Appl. Cryst. 14 (1981) 357–361, https://doi.org/10.1107/S0021889881009618.

[59] N. Fairley, CasaXPS: Spectrum Processing Software for XPS, AES and SIMS, Cheshire, 2006, http://www.casaxps.com.

[60] M. Mohai, Surf. Interface Anal. 36 (2004) 828–832.

[61] M. Mohai, XPS MultiQuant: Multi-model X-ray Photoelectron Spectroscopy Quantification Program, 2011. http://www.chemres.hu/aki/XMQpages/XMQhome.htm/.

[62] C.D. Wagner, A.V. Naumkin, A. Kraut-Vass, J.W. Allison, C.J. Powell, J.R. Rumble Jr., NIST X-ray Photoelectron Spectroscopy Database, Gaithersburg, MD, 2003, http://srdata.nist.gov/xps/.

[63] J. Moulder, W.F. Stickle, P.E. Sobol, K.D. Bomben, Handbook of X-ray Photoelectron Spectroscopy, Minnesota, Perkin Elmer Corporation, Minnesota, 1992.

[64] R. Woods, in: A.J. Bard (Ed.), Electroanalytical Chemistry: A Series of Advances, Vol. 9, Marcell Dekker, New York, 1976, pp. 1–162.

[65] M. Kang, H.K. Yoon, B.H. Kim, M.W. Song, C.H. Lee, React. Kinet. Catal. Lett. 80 (2003) 139–144, https://doi.org/10.1023/A:1026044511979.

[66] A. Magon, M. Pyda, Carbohydr. Res. 346 (16) (2011) 2558–2566, https://doi.org/10.1016/j.carres.2011.08.022.

[67] S. Mallakpour, M. Madani, J. Appl. Polym. Sci. (2015) 9, https://doi.org/10.1002/APP.42022.

[68] E. Peters, H. Mueller-Buschbaum, Zeitschrift fuer Naturforschung, Teil B. Anorganische Chemie, Organische Chemie 51 (1996) 29–31. Crystallography Open Database, www.crystallography.net/2002761.html.

[69] M.J. Lazaro, V. Celorrio, L. Calvillo, E. Pastor, R. Moliner, J. Power Sources 196 (2011) 4236–4241, https://doi.org/10.1016/j.jpowsour.2010.10.055.

[70] M. Carmo, A.R. dos Santos, J.G.R. Poco, M. Linardi, J. Power Sources 173 (2007) 860–866, https://doi.org/10.1016/j.jpowsour.2007.08.032.

[71] X. Zhang, M. Zhou, L. Lei, Carbon 43 (2005) 1700–1708, https://doi.org/10.1016/j.carbon.2005.02.013.

[72] C. Coromelci-Pastravanu, M. Ignat, E. Popovici, V. Harabagiu, J. Hazard. Mater. 278 (2014) 382–390, https://doi.org/10.1016/j.jhazmat.2014.06.036.

[73] K.S.W. Sing, R.T. Williams, Adsorpt. Sci. Technol. 22 (10) (2004) 773–782, https://doi.org/10.1260/0263617053499032.

[74] L. Stobinski, B. Lesiak, J. Zemek, P. Jiricek, Appl. Surf. Sci. 258 (2012) 7912–7917, https://doi.org/10.1016/j.apsusc.2012.04.127.

[75] Y. Yamada, H. Yasuda, K. Murota, M. Nakamura, T. Sodesawa, S. Sato, J. Mater. Sci. 48 (2013) 8171–8198, https://doi.org/10.1007/s10853-013-7630-0.

[76] Y. Li, Z. Yin, X. Liu, M. Cui, S. Chen, T. Ma, Mater. Today Chem. 19 (22) (2021) 100411, https://doi.org/10.1016/j.mtchem.2020.100411.

[77] J. Baltrusaitis, B. Mendoza-Sanchez, V. Fernandez, R. Veenstra, N. Dukstiene, A. Roberts, N. Fairley, Appl. Surf. Sci. 326 (2015) 151–161, https://doi.org/10.1016/j.apsusc.2014.11.077.

[78] D.O. Scanlon, G.W. Watson, D.J. Payne, G.R. Atkinson, R.G. Egdell, D.S.L. Law, J. Phys. Chem. C 114 (2010) 4636–4645, https://doi.org/10.1021/jp9093172.

[79] G. Samjeske, H. Wang, T. Löffler, H. Baltruschat, Electrochim. Acta 47 (2002) 3681–3692.

[80] R.A.M. Esfahani, S.K. Vankova, A.H.A. Monteverde Videla, S. Specchia, Appl. Catal. B-Environ. 201 (2017) 419–429, https://doi.org/10.1016/j.apcatb.2016.08.041.

[81] F. Maillard, S. Schreier, M. Hanzlik, E.R. Savinova, S. Weinkauf, U. Stimming, Phys. Chem. Chem. Phys. 7 (2005) 385–393, https://doi.org/10.1039/b411377b.

[82] F. Maillard, E. Peyrelade, Y. Soldo-Olivier, M. Chatenet, E. Chaînet, R. Faure, Electrochim. Acta 52 (2007) 1958–1967, https://doi.org/10.1016/j.electacta.2006.08.024.

[83] P. Justin, G.R. Rao, Int. J. Hydrogen Energy 36 (2011) 5875–5884, https://doi.org/10.1016/j.ijhydene.2011.01.122.

[84] O. Guillén-Villafuerte, G. García, J.L. Rodríguez, E. Pastor, R. Guil-López, E. Nieto, J.L.G. Fierro, Int. J. Hydrogen Energy 38 (2013) 7811–7821, https://doi.org/10.1016/j.ijhydene.2013.04.083.